Article

Kupffer cell programming by maternal obesity triggers fatty liver disease

https://doi.org/10.1038/s41586-025-09190-w

Received: 7 August 2023

Accepted: 23 May 2025

Published online: 18 June 2025

Open access

Check for updates

Hao Huang[1,23], Nora R. Balzer[1,23], Lea Seep[2], Iva Splichalova[1], Nelli Blank-Stein[1], Maria Francesca Viola[1], Eliana Franco Taveras[1], Kerim Acil[1], Diana Fink[3], Franzisca Petrovic[1], Nikola Makdissi[1], Seyhmus Bayar[1], Katharina Mauel[1], Carolin Radwaniak[1], Jelena Zurkovic[4], Amir H. Kayvanjoo[1], Klaus Wunderling[4], Malin Jessen[1], Mohamed H. Yaghmour[4], Lukas Kenner[5,6,7,8,9,10], Thomas Ulas[11,12,13], Stephan Grein[2], Joachim L. Schultze[11,12,13], Charlotte L. Scott[14,15], Martin Guilliams[14,16], Zhaoyuan Liu[17], Florent Ginhoux[17,18,19,20], Marc D. Beyer[11,13,21], Christoph Thiele[4], Felix Meissner[3], Jan Hasenauer[2], Dagmar Wachten[22] & Elvira Mass[1]✉

Kupffer cells (KCs) are tissue-resident macrophages that colonize the liver early during embryogenesis[1]. Upon liver colonization, KCs rapidly acquire a tissue-specific transcriptional signature, mature alongside the developing liver and adapt to its functions[1–3]. Throughout development and adulthood, KCs perform distinct core functions that are essential for liver and organismal homeostasis, including supporting fetal erythropoiesis, postnatal erythrocyte recycling and liver metabolism[4]. However, whether perturbations of macrophage core functions during development contribute to or cause disease at postnatal stages is poorly understood. Here, we utilize a mouse model of maternal obesity to perturb KC functions during gestation. We show that offspring exposed to maternal obesity develop fatty liver disease, driven by aberrant developmental programming of KCs that persists into adulthood. Programmed KCs promote lipid uptake by hepatocytes through apolipoprotein secretion. KC depletion in neonate mice born to obese mothers, followed by replenishment with naive monocytes, rescues fatty liver disease. Furthermore, genetic ablation of the gene encoding hypoxia-inducible factor-α (HIF1α) in macrophages during gestation prevents the metabolic programming of KCs from oxidative phosphorylation to glycolysis, thereby averting the development of fatty liver disease. These results establish developmental perturbation of KC functions as a causal factor in fatty liver disease in adulthood and position fetal-derived macrophages as critical intergenerational messengers within the concept of developmental origins of health and diseases[5].

Early-life environmental factors strongly influence the risk of developing non-communicable diseases in adulthood, a concept known as developmental origins of health and diseases (DOHaDs)[5]. Maternal malnutrition, obesity, infection, environmental pollutants and psychosocial stress have been associated with metabolic disorders, neurological diseases, cancer and dysregulated immune responses in offspring[6–11]. At the cellular level, maternal immune activation can alter fetal haematopoietic stem and progenitor cells (HSPCs), contributing to neonatal sepsis[12]. A maternal high-fat diet (HFD) or viral infection can also program microglia, the brain-resident macrophages, leading to neuronal disorders[9,13]. However, it remains elusive whether macrophages outside the brain can act as intergenerational messengers and causally contribute to disease onset, serving as cellular components in DOHaDs[7,8].

[1]Developmental Biology of the Immune System, Life and Medical Sciences (LIMES) Institute, University of Bonn, Bonn, Germany. [2]Computational Life Sciences, Life and Medical Sciences (LIMES) Institute and Bonn Center for Mathematical Life Sciences, University of Bonn, Bonn, Germany. [3]Institute of Innate Immunity, Department of Systems Immunology and Proteomics, Medical Faculty, University of Bonn, Bonn, Germany. [4]Biochemistry and Cell Biology of Lipids, Life and Medical Sciences (LIMES) Institute, University of Bonn, Bonn, Germany. [5]Clinical Institute of Pathology, Department for Experimental and Laboratory Animal Pathology, Medical University of Vienna, Vienna, Austria. [6]Comprehensive Cancer Center, Medical University Vienna, Vienna, Austria. [7]Unit of Laboratory Animal Pathology, University of Veterinary Medicine Vienna, Vienna, Austria. [8]Department of Molecular Biology, Umeå University, Umeå, Sweden. [9]Christian Doppler Laboratory for Applied Metabolomics, Medical University Vienna, Vienna, Austria. [10]Center for Biomarker Research in Medicine (CBmed), Graz, Austria. [11]Systems Medicine, Deutsches Zentrum für Neurodegenerative Erkrankungen (DZNE) e.V., Bonn, Germany. [12]Genomics and Immunoregulation, Life and Medical Sciences (LIMES) Institute, University of Bonn, Bonn, Germany. [13]PRECISE Platform for Single Cell Genomics and Epigenomics, DZNE and University of Bonn and West German Genome Center, Bonn, Germany. [14]Department of Biomedical Molecular Biology, Faculty of Science, Ghent University, Ghent, Belgium. [15]Laboratory of Myeloid Cell Biology in Tissue Damage and Inflammation, VIB-UGent Center for Inflammation Research, Ghent, Belgium. [16]Laboratory of Myeloid Cell Biology in Tissue Homeostasis and Regeneration, VIB-UGent Center for Inflammation Research, Ghent, Belgium. [17]Shanghai Institute of Immunology, Department of Immunology and Microbiology, Shanghai Jiao Tong University School of Medicine, Shanghai, China. [18]INSERM U1015, Gustave Roussy Cancer Campus, Villejuif, France. [19]Singapore Immunology Network, Agency for Science, Technology and Research, Singapore, Republic of Singapore. [20]Translational Immunology Institute, SingHealth Duke-NUS Academic Medical Centre, Singapore, Republic of Singapore. [21]Immunogenomics and Neurodegeneration, Deutsches Zentrum für Neurodegenerative Erkrankungen (DZNE) e.V., Bonn, Germany. [22]Institute of Innate Immunity, Biophysical Imaging, Medical Faculty, University of Bonn, Bonn, Germany. [23]These authors contributed equally: Hao Huang, Nora R. Balzer. ✉e-mail: elvira.mass@uni-bonn.de

Tissue-resident macrophages, including KCs in the liver, are long-lived, yolk sac-derived cells that support tissue development and homeostasis via production of growth factors, signalling molecules, and phagocytosis of waste products and apoptotic cells[4]. The liver, one of the first organs colonized by macrophages[1], exposes fetal KCs early to maternal blood components from the placenta[14]. Whether maternal environmental factors, particularly diet, influence KC development and functions, thereby leading to liver disease, remains unknown.

Metabolic dysfunction-associated fatty liver disease (MAFLD) is rising with global obesity[15]. MAFLD can progress to metabolic dysfunction-associated steatohepatitis, fibrosis and hepatocellular carcinoma. In diet-induced MAFLD, yolk sac-derived KCs can lose self-renewal and are, at least partially, replaced by monocyte-derived KC-like cells, diversifying the macrophage pool[16–19]. These macrophages adapt to the fatty liver environment, altering their epigenome and transcriptome, and contribute to disease progression through the secretion of inflammatory and non-inflammatory mediators[19,20]. Although our understanding of MAFLD and the role of KCs in disease progression to metabolic dysfunction-associated steatohepatitis is growing, it remains unclear how KCs respond to maternal obesity-induced fatty liver disease (FLD) in the offspring and whether they drive disease onset.

Here we show that maternal obesity induces a HIF1α-dependent metabolic reprogramming of yolk sac-derived KCs, persisting into adulthood and driving FLD. Using fate-mapping, depletion and conditional knockout (KO) models, combined with multi-omic profiling, we identified KCs as intergenerational messengers that translate maternal nutritional cues into long-lasting hepatic dysfunction. Our study uncovers a causal link between developmental KC perturbation and adult-onset FLD, positioning yolk sac-derived macrophages as central players in DOHaDs.

Maternal obesity causes fatty liver

Maternal obesity is associated with obesity and liver disease in offspring in humans and animal models[21], yet mechanisms remain unclear. We hypothesized that KCs may contribute to FLD due to their early liver colonization and metabolic roles[4]. To test this hypothesis, C57BL/6Jrcc female mice were fed a HFD for 8 weeks, leading to increased body weight and homeostatic model for insulin resistance (HOMA-IR; Extended Data Fig. 1a,b). These diet conditions did not lead to maternal inflammation as assessed by serum cytokine and chemokine measurements, with only interleukin-1α (IL-1α), C-C motif chemokine ligand 7 (CCL7) and leptin being upregulated (Extended Data Fig. 1c,d). Females were then bred to control diet (CD)-fed males. To dissect gestational versus lactational effects, newborn mice were cross-fostered and/or weaned onto a CD or HFD (Fig. 1a, maternal obese groups). As maternal lean control groups, we analysed offspring born to CD females and fed with a CD throughout life or weaned on a HFD (Fig. 1a). At 11 weeks, the maternal obese groups fed with a CD after birth (HFD_MCD_LCD; M denotes maternal diet during gestation and L refers to foster mother diet during lactating phase) or weaning (HFD_MHFD_LCD) showed no differences in body weight or white adipose tissue (WAT) weight compared with the maternal lean group on a CD (CD_MCD_LCD; Extended Data Fig. 1e). Only groups on a HFD postnatally (CD_MCD_LHFD, HFD_MCD_LHFD and HFD_MHFD_LHFD) developed obesity (Extended Data Fig. 1e), indicating that a post-weaning diet, not maternal obesity alone, determines overall body and WAT weight.

By contrast, liver lipid content increased in all maternal obese groups, as shown in the Oil-red-O (ORO) and haematoxylin and eosin (H&E) stainings, although the liver weight was similar in all conditions (Fig. 1b,c and Extended Data Fig. 1e,f). Both principal component analysis (PCA; Fig. 1d) and hierarchical clustering of lipidomics analyses (Extended Data Fig. 1g) indicated that maternal obese groups with a CD as their final diet (HFD>CD) were distinct from all animals fed a HFD as their final diet (CD>HFD and HFD>HFD), all of which diverge from CD_MCD_LCD (CD>CD). Indeed, the HFD_MCD_LCD and HFD_MHFD_LCD groups showed a significant increase of lipid species, such as saturated triacylglycerols, diacylglycerols and cholesterol esters, whereas maternal lean CD_MCD_LHFD as well as maternal obese HFD_MCD_LHFD and HFD_MHFD_LHFD groups showed only a moderate increase of lipid accumulation compared with CD_MCD_LCD livers.

We next performed serum metabolomics profiling of more than 900 metabolites and lipids to test whether the observed FLD phenotype of offspring born to obese mothers is also associated with systemic alterations, which might even serve as specific biomarkers. Group differences primarily reflected final dietary status (CD versus HFD; Extended Data Fig. 1h and Supplementary Table 1). Comparing CD_MCD_LCD with HFD_MCD_LCD offspring, in which body composition was similar but the FLD phenotype was most prominent in HFD_MCD_LCD livers, revealed 129 significantly altered metabolites (Supplementary Table 2), which were enriched in the metabolic pathways 'taurine and hypotaurine metabolism', 'arginine biosynthesis' and 'histidine metabolism' (Extended Data Fig. 1i). In particular, the glutamine:glutamate ratio, two amino acids that feed into arginine biosynthesis, was significantly increased in HFD_MCD_LCD mice (Supplementary Table 2). Although generally decreased in FLD[22], a maternal obesity model has reported an increased ratio correlating with liver metabolic state[23], suggesting a biomarker for maternal obesity-driven FLD. In summary, maternal obesity induces a distinct FLD phenotype in offspring compared with postnatal diet-induced FLD.

Maternal obesity reprograms KCs

We next characterized the maternal obesity-induced FLD phenotype focusing on hepatic myeloid cells, which have a critical role in FLD initiation and propagation[24]. Quantification confirmed increased neutrophils, monocytes and classical dendritic cells (cDC1 and cDC2) in HFD_MCD_LCD offspring (Extended Data Fig. 2a,b). KC numbers were increased across maternal obese groups, whereas liver capsular macrophages were unaffected. Post-weaning HFD in maternal lean controls (CD_MCD_LHFD) did not induce myeloid cell influx (Extended Data Fig. 2b). RNA sequencing (RNA-seq) on sorted KCs (Extended Data Fig. 2c) revealed clustering according to their in utero exposure to either lean (CD>) or obese (HFD>) mothers (Fig. 1e). Co-expression network analysis (hCo-Cena)[25] identified five modules (Fig. 1f and Supplementary Table 3). The steelblue module represented genes upregulated by maternal obesity. Pathway enrichment analyses using Gene Ontology (GO), Kyoto Encyclopedia of Genes and Genomes (KEGG) and HALLMARK databases revealed an upregulation of genes related to 'cell activation involved in immune response'. Among these genes was *Trem2*, which has been previously described to be upregulated in KCs during FLD[17], and which was accompanied by its downstream signalling cascade molecules *Tyrobp* and *Syk* in the same module (Fig. 1g). In addition, *Myd88*, *Gpnmb* and the monocyte-specific genes *Ccr2* and *Cx3cr1* were found in the steelblue module with the highest expression in HFD_MCD_LCD KCs (Fig. 1g). Moreover, we found the term 'glycolysis/gluconeogenesis' to be enriched in the steelblue module (Fig. 1f). By contrast, the turquoise and lightgreen modules indicated that metabolic processes such as 'oxidative phosphorylation', 'cellular respiration' and 'xenobiotic metabolism' were downregulated upon maternal obesity (Fig. 1f). Thus, maternal obesity causes an inflammatory response of KCs, and leads to an alteration of their metabolic status on a transcriptional level. To validate the transcriptional changes of KCs at the protein level, we performed spectral flow cytometry-based metabolic profiling[26] of KCs from CD_MCD_LCD and HFD_MCD_LCD offspring (Extended Data Fig. 2d). Although most nutrient transporters and metabolic enzymes involved in the glucose and lipid metabolic pathways remained unchanged, the enzyme succinate dehydrogenase (SDHA), a key component of the tricarboxylic acid cycle, and glucose transporter 1

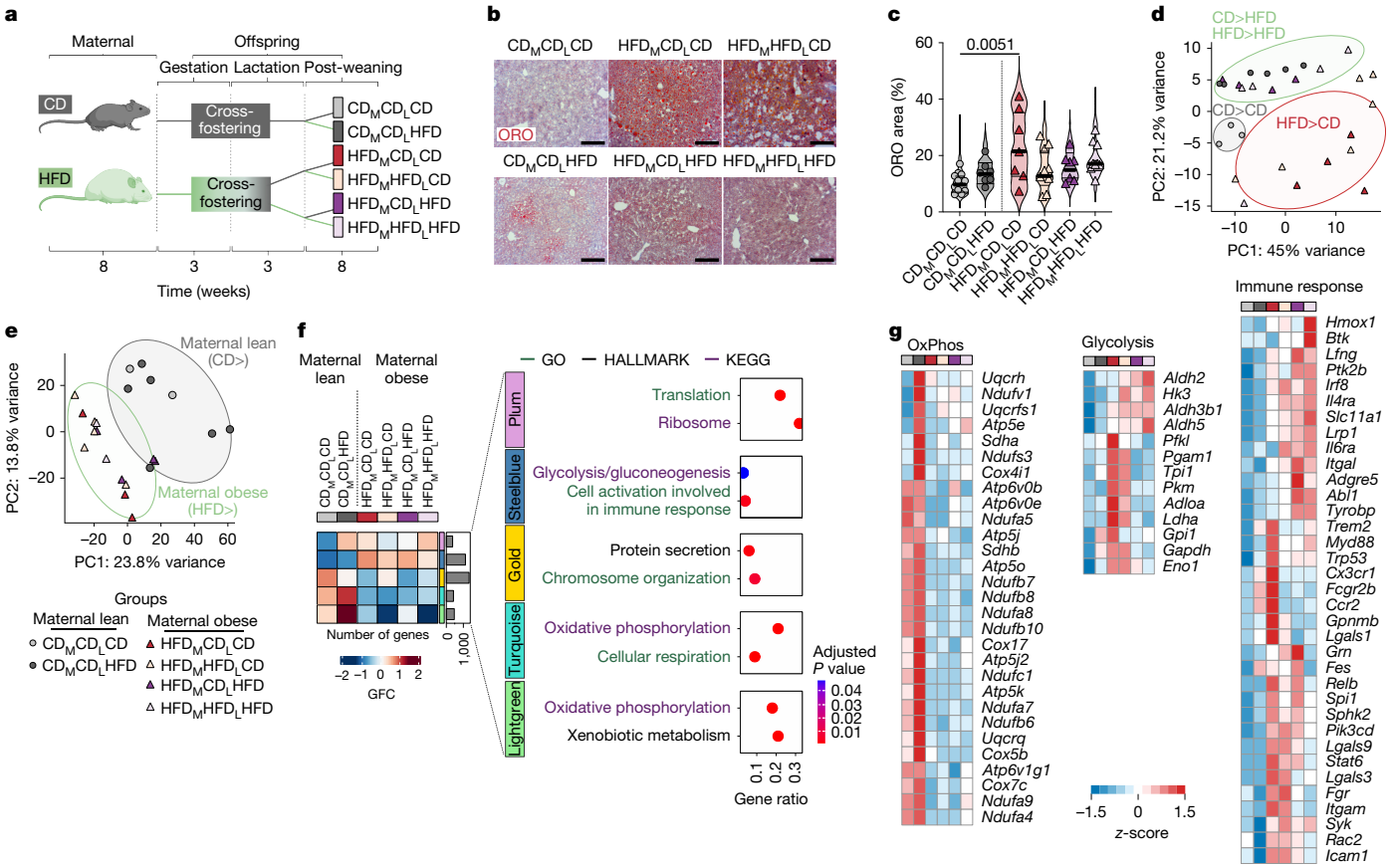

Fig. 1 | Maternal obesity leads to FLD in the offspring. a, Generation of the maternal obesity mouse model. **b**, ORO staining of offspring livers. Scale bars, 200 µm. Representative for $n = 11, 7, 7, 9, 7$ and 9 mice for CD_MCD_LCD, CD_MCD_LHFD, HFD_MCD_LCD, HFD_MHFD_LCD, HFD_MCD_LHFD and HFD_MHFD_LHFD groups, respectively, on 11 experimental days. **c**, ORO staining quantification of panel **b** by QuPath. Violin plots were created from 2–10 images per mouse, and the median and quartile of all images are shown. Each circle or triangle represents the mean of all the images per mouse. One-way analysis of variance (ANOVA) with Tukey's multiple comparison test, comparing the mean of all biological samples and showing significances of only CD_MCD_LCD, CD_MCD_LHFD and HFD_MCD_LCD groups, was used. **d**, Liver lipidomics of all experimental groups visualized by PCA. $n = 3, 6, 4, 6, 4$ and 5 mice for CD_MCD_LCD, CD_MCD_LHFD, HFD_MCD_LCD, HFD_MHFD_LCD, HFD_MCD_LHFD and HFD_MHFD_LHFD groups, respectively. **e**, Bulk RNA-seq analysis of sorted KCs visualized by PCA. Each circle or triangle represents one mouse. $n = 2, 6, 3, 5, 4$ and 2 mice for CD_MCD_LCD, CD_MCD_LHFD, HFD_MCD_LCD, HFD_MHFD_LCD, HFD_MCD_LHFD and HFD_MHFD_LHFD groups, respectively. **f**, Horizontal co-expression network analysis of KC RNA-seq data with the 5,000 most variable genes across all samples (left). The network was clustered, and group fold change (GFC) across all conditions per identified cluster is depicted. The selected enriched pathways of each horizontal co-expression network analysis module by over-representation analysis are also shown (right). $n = 2$–6 mice per group. **g**, Heatmap of selected genes of the intersection of DEGs and the respective annotated gene set from panel **f**. OxPhos, oxidative phosphorylation. Schematic in **a** created in BioRender. Mass, E. (2025) https://BioRender.com/3ecv7rv.

(GLUT1) were reduced in HFD_MCD_LCD KCs compared with CD_MCD_LCD (Extended Data Fig. 2e). These findings indicate that maternal obesity impairs the metabolic capacity of offspring KCs.

To determine systemic effects, we assessed serum cytokines and bone marrow compartment cellularity. No systemic cytokine elevation or progenitor changes were observed (Extended Data Fig. 3a–c). Together, maternal obesity-induced FLD is accompanied by local inflammation and a switch of KCs from oxidative phosphorylation to glycolysis.

KCs retain yolk sac origin

Diet-induced FLD models show increased monocyte influx and replacement of yolk sac-derived KCs[16–18]. Our RNA-seq data hinted at a monocyte signature in KCs from maternal obesity offspring. To address KC ontogeny, we generated *Tnfrsf11a*^{Cre};*Rosa26*$^{LSL\text{-}YFP}$;*Ms4a3*^{FlpO};*Rosa26*$^{FSF\text{-}tdTomato}$ mice. This double fate mapper allows to follow ontogeny of yolk sac-derived pre-macrophages and bone marrow-derived monocytes simultaneously using a combination of conventional recombinase approaches (Fig. 2a,b). We have previously shown that *Tnfrsf11a*^{Cre} mice label pre-macrophages and their progeny efficiently[1]. However, *Tnfrsf11a* is a core macrophage gene[1] whose expression is induced once monocytes differentiate into macrophages[27,28] whereby fetal-derived and bone marrow-derived macrophages remain undistinguishable. Thus, we additionally took advantage of the newly developed *Ms4a3*^{FlpO} mice (Extended Data Fig. 4a), as we previously have shown that the *Ms4a3* locus specifically targets monocytes and, thus, all monocyte-derived macrophages[29]. First, we confirmed that the fate-mapping efficiency of *Ms4a3*^{FlpO} mice was as efficient as in *Ms4a3*^{Cre} mice, with more than 95% Ly6C$^+$ blood monocytes being labelled with tdTomato (tdT; Extended Data Fig. 4b,c). Among these monocytes, we observed a small fraction (approximately 13%) that already expressed YFP, suggesting that these cells already start to express a core macrophage program. However, none of the monocytes was only YFP$^+$, demonstrating that the double fate mapper can unequivocally distinguish between the yolk sac-derived and adult bone marrow-derived waves of haematopoiesis (Extended Data Fig. 4c). High YFP labelling was also confirmed in microglia that are yolk sac derived[30,31] (Extended Data Fig. 4b,c). In 11–12-week-old CD_MCD_LCD livers, more than 96% of KCs were YFP$^+$, with minimal tdT labelling (less than 1% for YFP$^+$tdT$^+$ and approximately 3% for tdT$^+$; Fig. 2c and

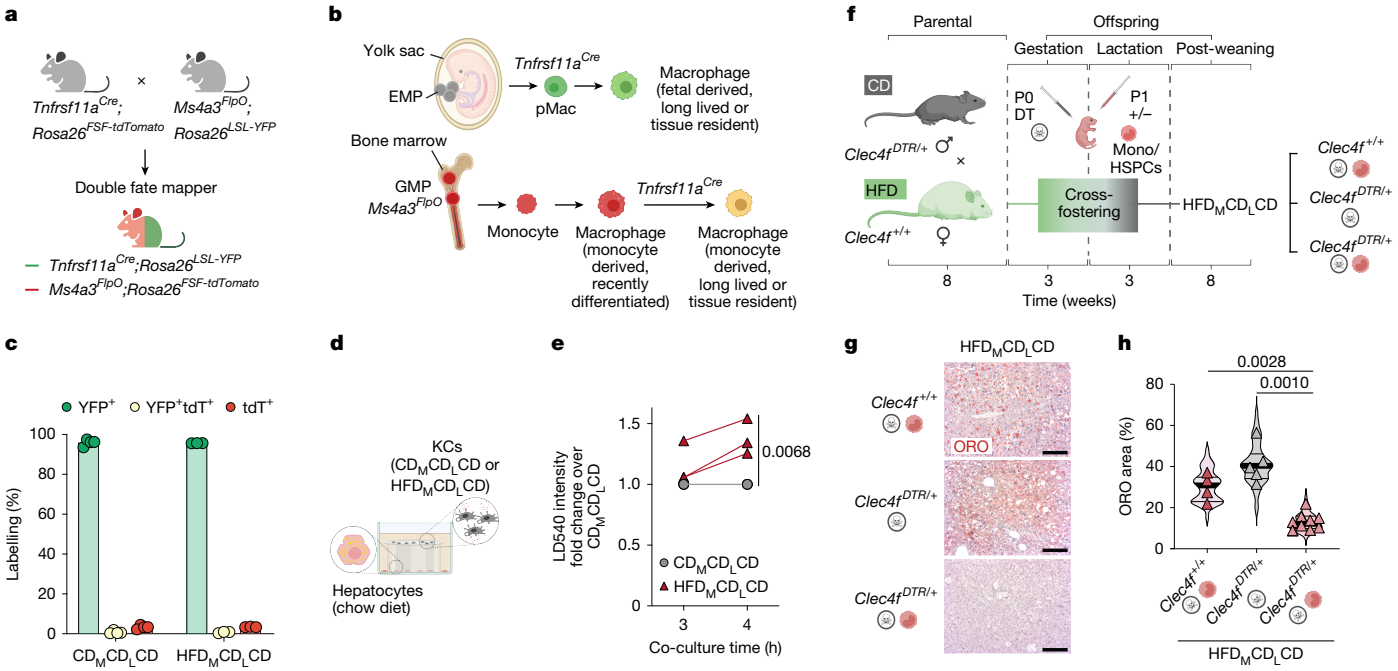

Fig. 2 | KCs retain yolk sac origin after maternal obesity and cause lipid droplet accumulation via paracrine signalling. a, Breeding scheme to generate *Tnfrsf11a*^{Cre};*Rosa26*$^{LSL\text{-}YFP}$;*Ms4a3*^{FlpO};*Rosa26*$^{FSF\text{-}tdTomato}$ double fate mapper mice. **b**, Schematic of lineage-tracing strategy of macrophages using the double fate mapper model. EMP, erythromyeloid progenitor; GMP, granulocyte–monocyte progenitor; pMac, pre-macrophage. Green indicates cells expressing YFP, red indicates tdT, and yellow indicates both YFP and tdT. **c**, Labelling efficiency of the double fate mapper model in KCs isolated from 11–12-week-old CD_MCD_LCD ($n = 4$ on 2 experimental days) and HFD_MCD_LCD ($n = 3$ on 2 experimental days) mice. The bar graphs show the mean ± s.d. **d**, Schematic of hepatocyte culture isolated from chow diet-fed mice with KC addition isolated from CD_MCD_LCD or HFD_MCD_LCD mice, respectively, which were recorded for lipid accumulation for a 4-h time course. **e**, Lipid accumulation shown by normalized LD540 intensity through live imaging in ex vivo-cultured hepatocytes co-cultured for 4 h with KCs from CD_MCD_LCD or HFD_MCD_LCD mice. $n = 3$ for CD_MCD_LCD or HFD_MCD_LCD mice with technical duplicates. Two-way ANOVA with Sidak's multiple comparison test on biological samples was used. **f**, Generation of KC depletion and cell transfer maternal obesity model. Diphtheria toxin (DT) indicated by the skull symbol. Monocyte and haematopoietic stem and progenitor cells (Mono/HSPCs) indicated by the red cell. **g**, Liver ORO staining in HFD_MCD_LCD offspring generated as shown in panel **f**. $n = 4$, 5 and 9 mice for *Clec4f*$^{+/+}$ with DT and Mono/HSPCs, *Clec4f*$^{DTR/+}$ with DT, *Clec4f*$^{DTR/+}$ with DT and Mono/HSPCs, respectively, on 7 experimental days. Scale bars, 200 µm. **h**, ORO staining quantification of panel **g** by QuPath. Violin plots were created from $n = 10$ images per mouse, and the median and quartile of all images are shown. Each triangle represents the mean of all images per mouse. A two-tailed Mann–Whitney test was used, comparing the mean of all biological samples. The illustrations of the mice in panel **a**, the schematics in panels **b**,**d**, the model in panel **f**, and the illustrations of the skull and red cell in panels **g**,**h** were created in BioRender. Mass, E. (2025) https://BioRender.com/5hrtyf4; https://BioRender.com/hh2dq2m; https://BioRender.com/hgceyko; https://BioRender.com/1don7ps.

Extended Data Fig. 4d), consistent with yolk sac origin[1,29]. Similarly, HFD_MCD_LCD KCs retained high YFP labelling (approximately 96%), despite the FLD phenotype and monocyte gene upregulation. Thus, KCs remain of yolk sac origin despite experiencing maternal obesity and a FLD environment during adulthood, and therefore can serve as intergenerational messengers conveying information that they experience in utero to adult life.

KC-derived factors cause lipid accumulation

We hypothesized that developmental programming of KCs by maternal obesity impairs their homeostatic function and promotes FLD via paracrine signalling. To test this hypothesis, we co-cultured hepatocytes with KCs from CD_MCD_LCD or HFD_MCD_LCD livers without direct cell contact, ensuring that only paracrine signalling occurred (Fig. 2d). Real-time lipid accumulation in hepatocytes was monitored using LD540 labelling to visualize neutral lipids via live-cell imaging. Hepatocytes co-cultured with HFD_MCD_LCD KCs exhibited significantly greater lipid accumulation, as indicated by increased LD540 intensity after 4 h, compared with those co-cultured with CD_MCD_LCD KCs (Fig. 2e). Thus, KCs that have experienced dietary factors from obese mothers during embryogenesis exert their FLD-promoting function via paracrine signalling.

To further validate KC-dependent lipid accumulation in hepatocytes in vivo, we utilized the KC–diphtheria toxin receptor (DTR) mouse model[32], in which human DTR is expressed under the control of the KC-specific *Clec4f* promoter, enabling targeted depletion of KCs within 24 h following a single dose of diphtheria toxin (Extended Data Fig. 5a,b). We generated HFD_MCD_LCD offspring with either the *Clec4f*$^{DTR/+}$ or *Clec4f*$^{+/+}$ genotype. At postnatal day 0 (P0), diphtheria toxin was injected to deplete KCs in *Clec4f*$^{DTR/+}$, followed by transplantation of tdT$^+$ bone marrow monocytes and HSPCs from naive mice at P1 to replenish the KC niche (Fig. 2f and Extended Data Fig. 5c). We confirmed the presence of tdT$^+$ KC-like cells in the adult liver of *Clec4f*$^{DTR/+}$ mice, despite a large fraction of KC-like cells originating also from endogenous tdT$^-$ progenitors (Extended Data Fig. 5d). This treatment effectively rescued the fatty liver phenotype in *Clec4f*$^{DTR/+}$ HFD_MCD_LCD mice, as evidenced by reduced lipid droplet accumulation in hepatocytes, demonstrated by ORO and H&E staining (Fig. 2g,h and Extended Data Fig. 5e). By contrast, *Clec4f*$^{+/+}$ littermates receiving the same diphtheria toxin injection and cell transfer retained lipid accumulation, consistent with observations in C57BL/6Jrcc mice (Fig. 1b,c). Moreover, replenishment of the empty KC niche solely by endogenous monocytes or HSPCs and residual KCs (*Clec4f*$^{DTR/+}$ mice injected with diphtheria toxin but without any cell transfer from a naive source), did not rescue the fatty liver phenotype (Fig. 2g,h and Extended Data Fig. 5e), indicating that HSPCs themselves may be developmentally programmed, as previously reported[33,34]. In summary, we demonstrate that KC-derived paracrine factors

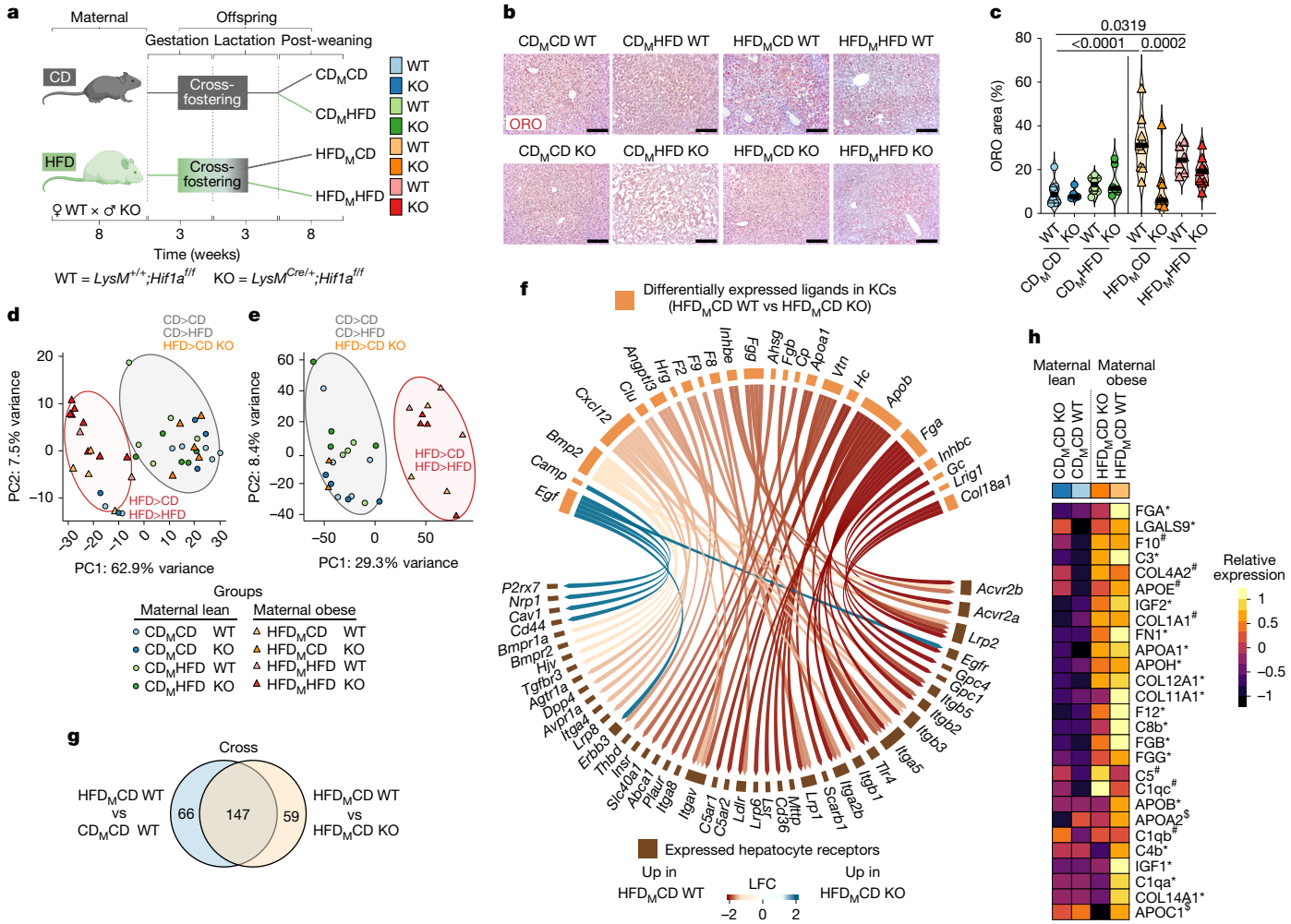

Fig. 3 | Postnatal FLD is driven by HIF1α-dependent developmental programming of KCs. a, Generation of the maternal obese model with myeloid *Hif1a* ablation. **b**, Representative liver ORO staining of $n = 8, 5, 8, 6, 9, 7, 6$ and 9 mice for CD_MCD WT, CD_MCD KO, CD_MHFD WT, CD_MHFD KO, HFD_MCD WT, HFD_MCD KO, HFD_MHFD WT and HFD_MHFD KO groups, respectively, on 15 experimental days. Scale bars, 200 µm. **c**, ORO staining quantification of panel **b** by QuPath. Violin plots were from $n = 1$–10 images per mouse, and the median and quartile of all images are shown. Each circle or triangle represents the mean of all images per mouse. One-way ANOVA with Tukey's multiple comparison test was used. **d**, Liver lipidomics visualized by PCA. $n = 7, 5, 5, 5, 4, 5, 3$ and 7 mice for CD_MCD WT, CD_MCD KO, CD_MHFD WT, CD_MHFD KO, HFD_MCD WT, HFD_MCD KO, HFD_MHFD WT and HFD_MHFD KO groups, respectively. **e**, Bulk RNA-seq analysis of sorted KCs visualized by PCA. $n = 5, 4, 4, 4, 3, 2, 3$ and 4 mice for CD_MCD WT, CD_MCD KO, CD_MHFD WT, CD_MHFD KO, HFD_MCD WT, HFD_MCD KO, HFD_MHFD WT and HFD_MHFD KO groups, respectively. **f**, Chord diagram showing KC ligands (in orange; DEGs between HFD_MCD WT and HFD_MCD KO in panel **e**) and their respective receptors (in brown) expressed by hepatocytes. LFC, log fold change. **g**, Venn diagram showing differentially expressed proteins from KCs comparing HFD_MCD WT versus CD_MCD WT (light blue), HFD_MCD WT versus HFD_MCD KO (light orange) mice, and overlapping proteins of the two comparisons ('Cross'). $n = 3, 3, 4$ and 3 mice for CD_MCD WT, CD_MCD KO, HFD_MCD WT and HFD_MCD KO groups, respectively, on 2 experimental days. **h**, Heatmap showing selected proteins from panel **g**. #HFD_MCD WT versus CD_MCD WT, HFD_MCD WT versus HFD_MCD KO and *Cross. ANOVA multiple-sample testing (S0 = 0.5, false discovery rate < 0.1 with 250 randomizations) was used. Schematic in **a** was created in BioRender. Mass, E. (2025) https://BioRender.com/lcxdcmf.

drive lipid accumulation in hepatocytes in the offspring of obese mothers.

HIF1α drives KC programming

As HIF1α regulates the metabolic switch of macrophages from oxidative phosphorylation to glycolysis[35,36], we tested whether preventing HIF1α-dependent developmental programming of KCs by maternal obesity would rescue the FLD phenotype. We used $LysM^{Cre}$;$Hif1a^{f/f}$ mice, in which *Hif1a* is depleted in macrophages and other myeloid cells[37]. As maternal diet during lactation showed minimal impact (Fig. 1), we focused on the dietary switch after birth in the maternal obese groups and used HFD-fed animals after weaning as control groups (Fig. 3a). Both $Hif1a^{f/f}$ (wild type (WT)) and $LysM^{Cre}$;$Hif1a^{f/f}$ (KO) littermates gained body weight and WAT weight when the end diet was a HFD (CD_MHFD and HFD_MHFD), indicating that myeloid-specific loss of HIF1α does not prevent diet-induced obesity (Extended Data Fig. 6a).

Next, we focused on the liver phenotype. As in the C57BL/6Jrcc mice, the total liver weight remained unaltered (Extended Data Fig. 6a), and $Hif1a^{f/f}$ offspring born to obese mothers (HFD_MCD WT) developed a FLD, as observed by ORO staining (Fig. 3b,c) and lipidomics (Fig. 3d and Extended Data Fig. 6b). Similar to the lipidomics results in C57BL/6Jrcc mice, HFD_MCD WT offspring showed an increase of saturated triacylglycerols and cholesterol esters. However, HFD_MCD KO offspring was rescued from developing a FLD (Fig. 3b–d and Extended Data Fig. 6b,c), indicating that depletion of HIF1α in KCs during embryogenesis is sufficient to prevent their metabolic programming, which ultimately drives lipid accumulation in hepatocytes. This effect was diminished

when KO offspring was kept on a HFD after birth (HFD_MHFD KO), as they showed a similar development of FLD as HFD_MHFD WT with high lipid accumulation (Fig. 3b,c) and significant increase of triacylglycerols, diacylglycerols, monoacylglycerol and cholesterol esters (Extended Data Fig. 6b). Hepatocyte transcriptomes reflected these differences (Extended Data Fig. 6d,e).

To assess a possible transient activation of HIF1α by maternal obesity specifically during gestation that may have long-lasting effects, we performed RNA-seq of KCs isolated from C57BL/6Jrcc mice at P0 born to CD-fed or HFD-fed mothers. Comparing differentially expressed genes (DEGs) from CD and HFD conditions resulted in 54 regulated genes (Extended Data Fig. 7a). To investigate gene regulation patterns, we inferred transcription factor activity on the basis of all DEGs and a collection of transcriptional regulatory interactions[38], indicating that DEGs were downstream of HIF1α, among other transcription factors (Extended Data Fig. 7b). Indeed, a total of five HIF1α target genes (*Hif3a*, *S100a8*, *S100a9*, *Tgfb3* and *Vegfa*) were among the 29 upregulated DEGs (Extended Data Fig. 7c), and HALLMARK analysis of these 29 upregulated DEGs revealed that they fall into the term 'hypoxia' (Extended Data Fig. 7d). Of note, only *Hif3a* expression was regulated, whereas genes encoding other HIF proteins were not transcriptionally regulated (Extended Data Fig. 7e). To validate that HIF1α is transiently active in KCs, we evaluated HIF1α protein expression in KCs of P0 neonate mice born to either HFD or CD mothers (Extended Data Fig. 7f). Quantification of immunofluorescence staining in the nucleus compared with the cytoplasm showed an increase of HIF1α translocation to the nucleus in maternal obese neonate mice when compared with maternal lean neonate mice (Extended Data Fig. 7g). These data indicate that KCs react to maternal obesity by increased HIF1α translocation to the nucleus, leading to the upregulation of HIF1α target genes at birth.

Together, our results show that the development of KCs from the offspring is perturbed by maternal obesity in a HIF1α-dependent manner, and that ablation of HIF1α function in fetal KCs rescues the development of FLD during adulthood caused by maternal obesity.

Maternal obesity rewires crosstalk

As FLD induced by maternal obesity was only rescued by *Hif1a* deletion if the offspring was kept on a CD, we asked whether additional factors, such as inflammation, may add to the hepatic lipid accumulation at postnatal stages when the offspring is fed with a HFD. To address whether hepatocytes may attract immune cells and cause a slowly increasing local inflammation in the liver when experiencing a HFD throughout life, we used the hepatocyte transcriptome data and investigated expression of chemoattractant factors. Indeed, we found *Agt* (encoding angiotensin), *C3* (encoding complement C3), *Lect2* (encoding leukocyte cell-derived chemotaxin 2) and *Cxcl12* (encoding C-X-C motif chemokine 12) to be particularly upregulated in hepatocytes isolated from HFD_MHFD WT and/or HFD_MHFD KO groups, which are involved in attracting monocytes and neutrophils[39–41] (Extended Data Fig. 8a). In line with these findings, flow cytometry analyses showed an, albeit not always significant, increase in the number of recruited myeloid cells (monocytes, neutrophils, cDC1 and cDC2; Extended Data Fig. 8b). Of note, deletion of *Hif1a* did not decrease myeloid cell numbers compared with WT littermates in any of the dietary conditions (Extended Data Fig. 8b), suggesting that the recruitment and/or proliferation of all myeloid cells is independent of HIF1α function at this early stage of FLD.

To investigate how HIF1α-dependent developmental programming in KCs causes FLD, we analysed the transcriptomes of WT and KO KCs from maternal lean and maternal obese conditions. PCA showed that maternal obesity, not the end diet, was the main driver of the KC transcriptional program (Fig. 3e), similar to the C57BL/6Jrcc model (Fig. 1e). Only KCs from HFD_MCD KO mice clustered with maternal lean conditions (Fig. 3e), demonstrating that developmental programming events caused by maternal obesity are HIF1α dependent. Focusing specifically on HIF1α-dependent gene regulation, comparing HFD_MCD WT versus HFD_MCD KO KCs, yielded 409 DEGs (adjusted *P* value of 0.1; Supplementary Table 4). GO term analysis of DEGs downregulated in HFD_MCD KO KCs revealed terms such as 'fatty acid metabolic process', 'cellular response to xenobiotic metabolism' and 'blood coagulation, fibrin clot formation' (Extended Data Fig. 8c and Supplementary Table 5). As ex vivo culture data indicated that KCs cause lipid accumulation via paracrine factors (Fig. 2d,e), we searched for secreted ligands with corresponding hepatocyte receptors. Among 25 differentially expressed ligands, the majority were upregulated in HFD_MCD WT compared with HFD_MCD KO KCs (Fig. 3f). Among them, we detected apolipoproteins (*Apob* and *Apoa1*) and many coagulation factors, such as *Fga*, *Fgb*, *Fgg*, *F2*, *F8* and *F9*, which encode fibrinogen, thrombin and coagulation factors VIII and IX, respectively.

To validate HIF1α-dependent upregulation of KC-derived ligands at the protein level, we performed proteomics on isolated KCs from CD_MCD WT, CD_MCD KO, HFD_MCD WT and HFD_MCD KO offspring. First, we compared HFD_MCD WT with CD_MCD WT to identify proteins induced by maternal obesity (WT list). Next, we compared HFD_MCD WT with HFD_MCD KO to identify HIF1α-dependent proteins in the context of maternal obesity (HFD_MCD list). These analyses identified 66 and 59 differentially expressed proteins, respectively, as well as 147 proteins that were both HIF1α dependent and induced by maternal obesity (Cross list; Fig. 3g and Extended Data Fig. 8d). GO, HALLMARK and KEGG analyses of these proteins revealed pathways such as 'triglyceride catabolic process', 'complement and coagulation cascades', 'insulin-like growth factor receptor signalling pathway' and 'ECM receptor interaction' among the Cross proteins. In addition, lipid transport pathways were enriched in the WT and HFD_MCD lists, whereas immune-related terms were specifically enriched in the HFD_MCD list (Extended Data Fig. 8e and Supplementary Table 6). A heatmap visualizing Cross proteins (Fig. 3h) showed that HIF1α deficiency in KCs prevented the upregulation of many proteins, including apolipoproteins and coagulation factors, in response to maternal obesity. Together, these transcriptional and proteomic analyses identified several HIF1α-dependent candidates induced by maternal obesity, potentially acting as KC-derived paracrine signals driving lipid accumulation in hepatocytes.

To determine whether maternal obesity-induced changes persist into adulthood and to avoid potential contamination from sorted KCs[42], we performed single-nucleus RNA (snRNA)-seq–assay for transposase-accessible chromatin using sequencing (ATAC-seq) on nuclei isolated from 12-week-old C57BL/6Jrcc $HFD_M$$CD_L$CD and $CD_M$$CD_L$CD offspring. This allowed for the epigenetic and transcriptomic analysis of individual cells. Integration of RNA-seq and ATAC-seq data resulted in various hepatic cell types, including KCs and hepatocytes (Extended Data Fig. 9a,b). Subclustering the KCs revealed five distinct KC states (Fig. 4a,b), with clusters 0, 1 and 4 expressing high levels of *Adgre1*, *Timd4* and *Clec4f*. Clusters 2 and 3, which increased relatively to the total KC numbers in the $HFD_M$$CD_L$CD condition, exhibited high levels of the MHC class II-related genes (*H2-Aa*, *H2-Ab1* and *Cd74*) in cluster 2 and immune-regulation and metabolic-response genes (*Pparg*, *Lilr4b* and *Lgals3*) in cluster 3 (Fig. 4b). Increased MHC class II expression was validated in the $HFD_M$$CD_L$CD liver parenchyma, whereas $CD_M$$CD_L$CD mice showed restricted MHC class II expression around the periportal and central veins of the liver (Extended Data Fig. 9c).

Comparisons of ATAC-seq peak-related genes between $HFD_M$$CD_L$CD and $CD_M$$CD_L$CD KCs identified 28 downregulated and 60 upregulated gene loci (Extended Data Fig. 9d). Despite the relatively low numbers, GO term analyses of downregulated genes indicated enrichment of lipid metabolic processes (Extended Data Fig. 9e). Of note, ATAC-seq peaks were differentially present within the *Pck1* locus, a gene encoding phosphoenolpyruvate carboxykinase 1, which is an enzyme that typically has an antagonistic role to glycolysis. Plotting the gene expression validated the loss of *Pck1* expression across all $HFD_M$$CD_L$CD KC states (Extended Data Fig. 9f), aligning with the metabolic switch described

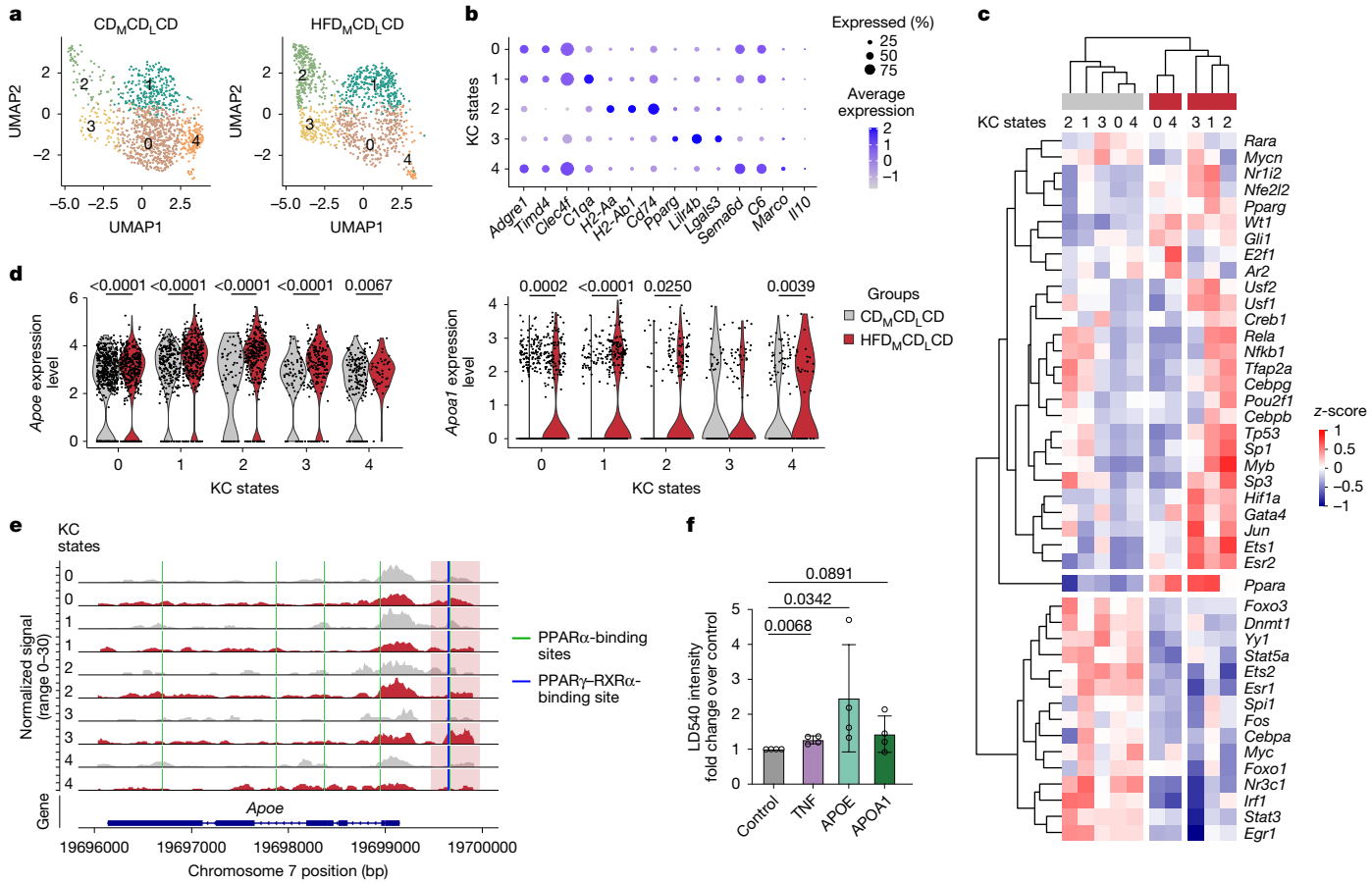

Fig. 4 | Maternal obesity induces epigenetic and transcriptional changes in the KCs of the offspring. a, snRNA/ATAC-seq of CD_MCD_LCD and HFD_MCD_LCD mice visualized by uniform manifold approximation and projection (UMAP) showing clusters depicting five different KC states. **b**, Dotplot showing genes specifically expressed by each KC state. **c**, Heatmap showing predicted transcription factor activity in each cluster of both CD_MCD_LCD and HFD_MCD_LCD groups. **d**, Violin plots comparing *Apoe* (left) and *Apoa1* (right) expression in all KC states between CD_MCD_LCD and HFD_MCD_LCD groups. Two-tailed Wilcoxon rank-sum test was used. **e**, ATAC-seq peak coverage plot of the *Apoe* locus comparing CD_MCD_LCD and HFD_MCD_LCD groups for each KC state. A possible differentially exploited regulatory region controlling *Apoe* expression is highlighted in red. Transcription factor-binding sites of PPARγ–RXRα are highlighted with a blue vertical line and of PPARα with green vertical lines. **f**, Lipid accumulation shown by normalized LD540 intensity through live imaging in ex vivo-cultured hepatocytes supplemented without any factor (control), with TNF, APOE or APOA1. $n = 4$ mice per group with technical triplicates. Mean ± s.d. of biological samples is shown. One-tailed ratio paired Student's *t*-test on biological samples comparing treated groups to control was used.

earlier (Fig. 1f,g and Extended Data Fig. 2d,e). Furthermore, we observed epigenetic changes within the *Gpnmb* locus where ATAC-seq peaks increased significantly. Of note, *Gpnmb* has been previously described as a biomarker for steatohepatitis[43]. Consistent with bulk RNA-seq results, this epigenetic change was accompanied by upregulation of *Gpnmb* gene expression (Extended Data Fig. 9d,f). However, this upregulation was restricted only to clusters 2 and 3, which expand proportionally under maternal obesity conditions. To investigate whether these distinct KC states are differentially regulated at the transcriptional level, we performed DEG analysis comparing the clusters (Supplementary Table 7), combined with DecoupleR transcription factor activity analysis. This revealed that KC states clustered by dietary condition rather than identity, indicating that persistent changes in transcription factor activity were driving the observed DEGs in HFD_MCD_LCD KCs (Fig. 4c). Transcription factor activity analysis identified HIF1α to be mainly active in clusters 1, 2 and 3 in the HFD_MCD_LCD condition. Transcription factors, such as Jun, Ets1 and Esr2, were more active in most HFD_MCD_LCD clusters, with PPARα and PPARγ showing increased activity across all HFD_MCD_LCD clusters (Fig. 4c). These findings suggest that, in addition to HIF1α, other persistent transcriptional changes stem from altered transcription factor activity in offspring born to obese mothers.

Next, we leveraged the snRNA-seq data to assess signalling pathways that are activated in HFD_MCD_LCD KCs using CellChat analysis. In line with the bulk RNA-seq data, KCs demonstrated increased intercellular communication via APOE and APOA1 signalling pathways under maternal obesity conditions (Extended Data Fig. 9g). Gene expression analyses confirmed upregulation of *Apoe* and *Apoa1* in all HFD_MCD_LCD states (Fig. 4d), consistent with increased transcription factor activity of PPARα and PPARγ, which are known regulators of apolipoproteins[44]. In addition, ATAC-seq analysis revealed an increase in peaks at putative regulatory elements located upstream of the *Apoe* promoter in HFD_MCD_LCD cluster 3 compared with CD_MCD_LCD, which harbour PPARα and PPARγ–RXRα transcription factor-binding sides (Fig. 4e).

Together, our data show that maternal obesity induces persistent changes in KCs. Of note, we identified new KC states (clusters 2 and 3) that probably account for the immune-related signature observed in the bulk RNA-seq data. These clusters expand in response to maternal obesity and specifically upregulate inflammatory genes. Furthermore, the snRNA–ATAC-seq approach corroborates our findings from bulk RNA-seq and proteomics approaches, highlighting the significant upregulation of apolipoproteins in KCs.

To investigate whether apolipoproteins contribute to lipid accumulation in the liver, we utilized the hepatocyte live-imaging cell culture

approach, adding APOE or APOA1 to the medium. As a positive control, we used tumour necrosis factor (TNF), which has been previously identified as a KC-derived driver of lipid storage in hepatocytes[45]. In all conditions, the LD540 signal intensity increased, with APOE inducing the highest lipid accumulation compared with control hepatocytes (Fig. 4f).

In summary, our findings provide evidence that HIF1α-dependent developmental programming by maternal obesity leads to the upregulation of apolipoproteins in adult KCs, which can induce lipid accumulation in hepatocytes, thereby contributing to the onset of FLD.

Discussion

This work supports the hypothesis that yolk sac-derived tissue-resident macrophages are cellular components within the concept of DOHaDs, as developmental perturbations of hepatic macrophages result in postnatal liver pathophysiology. This is in line with previous studies showing that microglia can contribute to neurodevelopmental and behavioural disorders[8,9,46–48]. Our data indicate that continuous exposure to a maternal HFD during gestation induces a HIF1α-dependent metabolic switch in KCs from oxidative phosphorylation to glycolysis, detrimentally affecting adult hepatic lipid metabolism. Unlike most maternal immune activation studies, in which cytokines such as IL-6 and IL-17a influence offspring development[49,50], our model does not indicate a maternal immune activation phenotype or systemic inflammation. Instead, maternal metabolites and lipids probably cross the placenta and modulate macrophage function. For instance, stearic acid, enriched in obese mice, has been proposed to reprogram macrophages via Toll-like receptor 4 (TLR4)[9,51]. An intriguing question for future research is to administer defined fatty acids to pregnant dams and trace their effect on fetal KC development in a HIF1α-dependent manner.

Using the *LysM*^{Cre} mouse model to delete *Hif1a* specifically in myeloid cells excludes developmental programming of oocytes, hepatocytes and their progenitors as primary driver of FLD, as the promotor controlling expression of the Cre recombinase only becomes active during early fetal macrophage differentiation[1,52]. However, indirect effects via inter-organ communication, such as adipose-derived signals, cannot be ruled out. Our double fate mapper model showed that KCs remain of yolk sac origin upon maternal obesity, contrasting with diet-induced FLD models in which bone marrow-derived cells replace KCs[16–18]. Thus, in accordance with DOHaDs, KCs can serve as intergenerational messengers that sense maternal-derived factors during gestation and convey this information into a long-lasting transcriptional program during adulthood. Our transcriptomic, epigenetic and metabolic analyses demonstrate that maternal obesity functionally programs KCs, promoting lipid accumulation in neighbouring hepatocytes via persistent transcriptional changes. KC depletion experiments further confirmed this: replenishment with monocyte-derived cells from animals that never experienced a HFD rescues the developmental programming effects, providing a potential cellular target for treating FLD caused by maternal obesity. Replenishment with monocytes from maternal obesity-experienced animals did not rescue the phenotype, suggesting that neonatal monocytes or HSPCs undergo developmental programming[33,34]. These findings highlight the resilience of the KC niche to maternal obesity-induced programming, as the origin of KC-like cells determines FLD pathogenesis.

A previous study has shown that upon a postnatal HFD, KCs secrete pro-inflammatory factors, such as IL-1β, IL-6 and TNF, with TNF inducing lipid accumulation in hepatocytes[45]. By contrast, in maternal obesity-induced FLD, we observed no upregulation of these particular factors. Instead, genes associated with lipid metabolism (for example, *Trem2, Tyrobp*, *Syk* and *Lpr1*) were upregulated, partially resembling the phenotype of hepatic lipid-associated macrophages (LAMs)[17]. Recent work has also shown that TREM2^{+} LAMs expand during injury and can originate from both resident KCs and monocyte-derived macrophages[53]. In our model, however, LAM-like KCs remain of yolk sac origin, suggesting that functional adaptation to lipid-rich environments, rather than a change in cellular origin, drives their phenotype. This distinction highlights the unique nature of maternal obesity-induced FLD compared with postnatal HFD models. Notably, maternal obesity upregulates apolipoproteins such as APOE and APOA1 in a HIF1α-dependent manner, aligning with previous findings linking apolipoproteins with FLD[54,55].

In summary, our study establishes KCs as active players in liver metabolism, demonstrating distinct responses to a maternal-derived versus postnatal diet-derived HFD. We showed that a maternal HFD during gestation programs KCs metabolically and transcriptionally in a HIF1α-dependent manner, leading to persistent changes that promote FLD. These findings offer a therapeutic time window to manipulate the metabolic status of KCs, and thereby prevent the development of FLD in the offspring.

Online content

Any methods, additional references, Nature Portfolio reporting summaries, source data, extended data, supplementary information, acknowledgements, peer review information; details of author contributions and competing interests; and statements of data and code availability are available at https://doi.org/10.1038/s41586-025-09190-w.

1. Mass, E. et al. Specification of tissue-resident macrophages during organogenesis. *Science* **353**, aaf4238 (2016).
2. Gosselin, D. et al. Environment drives selection and function of enhancers controlling tissue-specific macrophage identities. *Cell* **159**, 1327–1340 (2014).
3. Okabe, Y. & Medzhitov, R. Tissue-specific signals control reversible program of localization and functional polarization of macrophages. *Cell* **157**, 832–844 (2014).
4. Mass, E., Nimmerjahn, F., Kierdorf, K. & Schlitzer, A. Tissue-specific macrophages: how they develop and choreograph tissue biology. *Nat. Rev. Immunol.* https://doi.org/10.1038/s41577-023-00848-y (2023).
5. Barker, D. J. P. The developmental origins of chronic adult disease. *Acta Paediat. Suppl.* https://doi.org/10.1080/08035320410022730 (2004).
6. Barker, D. J. P., Osmond, C., Kajantie, E. & Eriksson, J. G. Growth and chronic disease: findings in the Helsinki birth cohort. *Ann. Hum. Biol.* **36**, 445–458 (2009).
7. Mass, E. & Gentek, R. Fetal-derived immune cells at the roots of lifelong pathophysiology. *Front. Cell Dev. Biol.* **9**, 648313 (2021).
8. Viola, M. F., Franco Taveras, E. & Mass, E. Developmental programming of tissue-resident macrophages. *Front. Immunol.* https://doi.org/10.3389/fimmu.2024.1475369 (2024).
9. Ceasrine, A. M. et al. Maternal diet disrupts the placenta–brain axis in a sex-specific manner. *Nat. Metab.* **4**, 1732–1745 (2022).
10. Roseboom, T. J. et al. Effects of prenatal exposure to the Dutch famine on adult disease in later life: an overview. *Mol. Cell. Endocrinol.* **185**, 93–98 (2001).
11. Ravelli, G.-P., Stein, Z. A. & Susser, M. W. Obesity in young men after famine exposure in utero and early infancy. *N. Engl. J. Med.* https://doi.org/10.1056/nejm197608122950701 (2010).
12. Collins, A. et al. Maternal inflammation regulates fetal emergency myelopoiesis. *Cell* **187**, 1402–1421.e21 (2024).
13. Knuesel, I. et al. Maternal immune activation and abnormal brain development across CNS disorders. *Nat. Rev. Neurol.* **10**, 643–660 (2014).
14. Aplin, J. D., Myers, J. E., Timms, K. & Westwood, M. Tracking placental development in health and disease. *Nat. Rev. Endocrinol.* **16**, 479–494 (2020).
15. Teng, M. L. P. et al. Global incidence and prevalence of nonalcoholic fatty liver disease. *Clin. Mol. Hepatol.* **29**, S32–S42 (2022).
16. Tran, S. et al. Impaired Kupffer cell self-renewal alters the liver response to lipid overload during non-alcoholic steatohepatitis. *Immunity* **53**, 627–640.e5 (2020).
17. Remmerie, A. et al. Osteopontin expression identifies a subset of recruited macrophages distinct from Kupffer cells in the fatty liver. *Immunity* **53**, 641–657.e14 (2020).
18. Seidman, J. S. et al. Niche-specific reprogramming of epigenetic landscapes drives myeloid cell diversity in nonalcoholic steatohepatitis. *Immunity* https://doi.org/10.1016/j.immuni.2020.04.001 (2020).
19. Guilliams, M. & Scott, C. L. Liver macrophages in health and disease. *Immunity* **55**, 1515–1529 (2022).
20. Morgantini, C. et al. Liver macrophages regulate systemic metabolism through non-inflammatory factors. *Nat. Metab.* **1**, 445–459 (2019).
21. Brumbaugh, D. E. & Friedman, J. E. Developmental origins of nonalcoholic fatty liver disease. *Pediatr. Res.* **75**, 140–147 (2013).
22. Delgado, T. C., de las Heras, J. & Martínez-Chantar, M. L. Understanding gut–liver axis nitrogen metabolism in fatty liver disease. *Front. Endocrinol.* **13**, 3173 (2022).
23. Hinrichs, H., Faerber, A., Young, M., Ballentine, S. J. & Thompson, M. D. Maternal exercise protects male offspring from maternal diet programmed non-alcoholic fatty liver disease progression. *Endocrinology* **164**, bqad010 (2023).
24. Huby, T. & Gautier, E. L. Immune cell-mediated features of non-alcoholic steatohepatitis. *Nat. Rev. Immunol.* **22**, 429–443 (2021).
25. Oestreich, M. et al. hCoCena: horizontal integration and analysis of transcriptomics datasets. *Bioinformatics* **38**, 4727–4734 (2022).
26. Heieis, G. A. et al. Metabolic heterogeneity of tissue-resident macrophages in homeostasis and during helminth infection. *Nat. Commun.* **14**, 5627 (2023).

27. Hume, D. A., Summers, K. M. & Rehli, M. Transcriptional regulation and macrophage differentiation. *Microbiol. Spectr.* https://doi.org/10.1128/microbiolspec.mchd-0024-2015 (2016).
28. Kido, S. et al. Expression of RANK is dependent upon differentiation into the macrophage/osteoclast lineage: induction by 1α,25-dihydroxyvitamin D3 and TPA in a human myelomonocytic cell line, HL60. *Bone* **32**, 621–629 (2003).
29. Liu, Z. et al. Fate mapping via Ms4a3-expression history traces monocyte-derived cells. *Cell* **178**, 1509–1525.e19 (2019).
30. Alliot, F., Godin, I. & Pessac, B. Microglia derive from progenitors, originating from the yolk sac, and which proliferate in the brain. *Dev. Brain Res.* **117**, 145–152 (1999).
31. Ginhoux, F. et al. Fate mapping analysis reveals that adult microglia derive from primitive macrophages. *Science* **330**, 841–845 (2010).
32. Scott, C. L. et al. Bone marrow-derived monocytes give rise to self-renewing and fully differentiated Kupffer cells. *Nat. Commun.* **7**, 10321 (2016).
33. Kamimae-Lanning, A. N. et al. Maternal high-fat diet and obesity compromise fetal hematopoiesis. *Mol. Metab.* **4**, 25–38 (2015).
34. Sureshchandra, S. et al. Maternal Western-style diet remodels the transcriptional landscape of fetal hematopoietic stem and progenitor cells in rhesus macaques. *Stem Cell Rep.* https://doi.org/10.1016/j.stemcr.2022.10.003 (2022).
35. Taylor, C. T. & Scholz, C. C. The effect of HIF on metabolism and immunity. *Nat. Rev. Nephrol.* **18**, 573–587 (2022).
36. Cramer, T. et al. HIF-1α is essential for myeloid cell-mediated inflammation. *Cell* **112**, 645–657 (2003).
37. Clausen, B. E., Burkhardt, C., Reith, W., Renkawitz, R. & Förster, I. Conditional gene targeting in macrophages and granulocytes using LysMcre mice. *Transgenic Res.* **8**, 265–277 (1999).
38. Müller-Dott, S. et al. Expanding the coverage of regulons from high-confidence prior knowledge for accurate estimation of transcription factor activities. *Nucleic Acids Res.* **51**, 10934–10949 (2023).
39. Yamagoe, S. et al. Purification and primary amino acid sequence of a novel neutrophil chemotactic factor LECT2. *Immunol. Lett.* **52**, 9–13 (1996).
40. Ruiz-Ortega, M. et al. Angiotensin II participates in mononuclear cell recruitment in experimental immune complex nephritis through nuclear factor-κB activation and monocyte chemoattractant protein-1 synthesis. *J. Immunol.* **161**, 430–439 (1998).
41. Metzemaekers, M., Gouwy, M. & Proost, P. Neutrophil chemoattractant receptors in health and disease: double-edged swords. *Cell. Mol. Immunol.* **17**, 433–450 (2020).
42. Lynch, R. W. et al. An efficient method to isolate Kupffer cells eliminating endothelial cell contamination and selective bias. *J. Leukoc. Biol.* **104**, 579–586 (2018).
43. Katayama, A. et al. Beneficial impact of Gpnmb and its significance as a biomarker in nonalcoholic steatohepatitis. *Sci. Rep.* **5**, 16920 (2015).
44. Fuior, E. V. et al. Peroxisome proliferator-activated receptor α in lipoprotein metabolism and atherosclerotic cardiovascular disease. *Biomedicines* **11**, 2696 (2023).
45. Diehl, K. L. et al. Kupffer cells sense free fatty acids and regulate hepatic lipid metabolism in high-fat diet and inflammation. *Cells* **9**, 2258 (2020).
46. Block, C. L. et al. Prenatal environmental stressors impair postnatal microglia function and adult behavior in males. *Cell Rep.* https://doi.org/10.1016/j.celrep.2022.111161 (2022).
47. Han, V. X., Patel, S., Jones, H. F. & Dale, R. C. Maternal immune activation and neuroinflammation in human neurodevelopmental disorders. *Nat. Rev. Neurol.* **17**, 564–579 (2021).
48. Bilbo, S. D. & Schwarz, J. M. Early-life programming of later-life brain and behavior: a critical role for the immune system. *Front. Behav. Neurosci.* **3**, 670 (2009).
49. Hsiao, E. Y. & Patterson, P. H. Activation of the maternal immune system induces endocrine changes in the placenta via IL-6. *Brain Behav. Immun.* **25**, 604–615 (2011).
50. Otero, A. M. & Antonson, A. M. At the crux of maternal immune activation: viruses, microglia, microbes, and IL-17A. *Immunol. Rev.* **311**, 205–223 (2022).
51. Hata, M. et al. Past history of obesity triggers persistent epigenetic changes in innate immunity and exacerbates neuroinflammation. *Science* **379**, 45–62 (2023).
52. Kierdorf, K. et al. Microglia emerge from erythromyeloid precursors via Pu.1- and Irf8-dependent pathways. *Nat. Neurosci.* **16**, 273–280 (2013).
53. De Ponti, F. F. et al. Spatially restricted and ontogenically distinct hepatic macrophages are required for tissue repair. *Immunity* **58**, 362–380.e10 (2025).
54. Jiang, Z. G., Robson, S. C. & Yao, Z. Lipoprotein metabolism in nonalcoholic fatty liver disease. *J. Biomed. Res.* **27**, 1–13 (2013).
55. Nascimento, J. C. R. et al. Impact of apolipoprotein E genetic polymorphisms on liver disease: an essential review. *Ann. Hepatol.* **19**, 24–30 (2020).

Methods

Mice

All investigations concerning mouse work had local approval and all procedures conformed to the guidelines from Directive 2010/63/EU of the European Parliament on protecting animals used for scientific purposes. In detail, all animal experiments were conducted according to the German law of animal protection and in agreement with the approval of the local institutional animal care committee (Landesamt für Natur, Umwelt und Verbraucherschutz (LANUV), North Rhine-Westphalia, Az 81-02.04.2019.A146 and Az 2024-A314). Mice were housed under specific pathogen-free conditions with 12-h light–dark cycle, at 21 °C, 55% relative humidity, and with food and water provided ad libitum. Animals were euthanized using liver or heart perfusion after anaesthesia injection. C57BL/6JRcc was used as the WT strain. To generate the double fate mapper *Tnfrsf11a*^{Cre} (ref. 56); *Rosa26*$^{LSL\text{-}YFP}$ (JAX stock #006148)[57]; *Ms4a3*^{FlpO};*Rosa26*$^{FSF\text{-}tdT}$ (JAX stock #032864)[58], we bred *Tnfrsf11a*$^{Cre/+}$;*Rosa26*$^{FSF\text{-}tdT/FSF\text{-}tdT}$ animals with *Ms4a3*^{FlpO};*Rosa26*$^{LSL\text{-}YFP/LSL\text{-}YFP}$ animals (see Extended Data Fig. 4a for description of the *Ms4a3*^{FlpO} locus). KC-DTR (*Clec4f*$^{DTR/+}$) mice have been previously described[32]. All mice were originally of the C57BL/6J background and crossed to C57BL/6Jrcc for 2–5 generations. To generate *Hif1a*$^{flox/flox}$;*LysM*$^{Cre/+}$, the *Hif1a*$^{flox/flox}$ (JAX stock #007561)[59] and *LysM*$^{Cre/+}$ (JAX stock #004781)[37] were used (both kept on the C57BL/6J background after import). All lines were back-crossed to their respective WT line (C57BL/6J for *LysM*$^{Cre/+}$;*Hif1a*$^{flox/flox}$ and C57BL/6Jrcc for all other lines) once per year. Mice were genotyped according to protocols provided by JAX or donating researchers. For all experiments, male mice were analysed with the exception of the double fate mapper, where both male and female mice were used, and ex vivo-isolated hepatocytes, where only young female mice were used to assure a lean and metabolically healthy state.

Mouse maternal obesity model

For WT cohorts, 3–4-week-old C57BL/6JRcc female mice were put on a CD (sniff, E15748-047) for 2 weeks. Subsequently, female mice were separated into two groups and received either a HFD (sniff, E15742-347) or a CD for 8 weeks. For metabolic assessment, the HOMA-IR was used[60]. Glucose was measured using GlucoCheck GOLD with stripes (11864873 and 11864933), and insulin was measured via ELISA (EMINS, Thermo Fisher). Only mice with significantly higher HOMA-IR were used to generate offspring. Females were mated with males fed with a CD overnight. The day of vaginal plug formation was estimated as embryonic developmental day 0.5 (E0.5) post-coitum. Females were always placed back in their cages with a HFD after overnight mating. All offspring were cross-fostered to females on the respective diet. The litter size was standardized to a maximum of six pups per foster mother on the day of birth. In addition, whenever possible, litters from different biological mothers were cross-fostered to the same foster mother to ensure consistency and minimize maternal variability. Cross-fostering took place also between mothers on the same diet to exclude stress-mediated effects of cross-fostering. After 3 weeks of lactation at postnatal day 21 (P21), offspring were weaned into their post-weaning cage (CD or HFD). Here offspring from maternal lean and maternal obese groups were mixed to minimize effects caused by cage-specific microbiome differences. In addition, during the post-weaning diet, bedding stemming from cages with the same diet was mixed weekly between cages (typically 10–20 cages at any time) to further reduce cage-specific effects related to the microbiome.

Mice were euthanized and used in the experiment at weeks 11–13, unless otherwise stated.

Adoptive transfer of KCs for KC-DTR mice

Maternal obese KC-DTR male offspring were injected at P0 with 50 ng diphtheria toxin and injected at P1 through the temporal vein under ice-induced anaesthesia with 10^6 bone marrow monocytes and HSPCs isolated from *Rosa26*^{mTmG} mice. Bone marrow monocytes and HSPCs were isolated as following: *Rosa26*^{mTmG} mice were killed through cervical dislocation, and their tibias and femurs from the hindlimbs were freed. Bone marrow was flushed out with DMEM (Pan Biotech) and filtered through a 70-µm strainer on ice. Cells were then blocked with FACS buffer (0.5% BSA and 2 mM EDTA in PBS) containing 2% rat serum and stained with biotinylated antibodies (anti-Ly6G, CD19, CD3, Ter119, Nkp45 and F4/80) for 30 min at 4 °C. Monocytes and HSPCs were then negatively selected using MojoSort Streptavidin Nanobeads (BioLegend) following the manufacturer's manual.

Preparation of cell suspension for flow cytometry and cell sorting

Adult mice were anaesthetized and perfused with ice-cold PBS. P0 mice were killed by decapitation. For flow cytometry analysis of hepatic myeloid cells, 200–300 mg of adult or half of a P0 liver was collected, cut into small pieces and incubated in a digestion mix (PBS containing 1 mg ml^{-1} collagenase D (11088858001, Roche), 100 U ml^{-1} DNase I (DN25, Sigma-Aldrich), 2.4 mg ml^{-1} of dispase (17105041, Gibco) and 3% fetal calf serum (FCS; Invitrogen) for 30 min at 37 °C before mechanical disruption through a 100-µm filter. The cell suspension was diluted in 3 ml of FACS buffer (0.5% BSA and 2 mM EDTA in PBS) and centrifuged at 50*g* for 3 min to remove hepatocytes. Then, the supernatant containing myeloid cells was collected and centrifuged at 370*g* for 7 min at 4 °C. For bone marrow, one leg was isolated, and both the tibia and the femur were cleaned from surrounding tissues and cut at the ends. The bones were flushed with 5 ml of ice-cold FACS buffer. Cells were centrifuged at 370*g* for 7 min at 4 °C. Pellet was resuspended in red blood cell lysis buffer (155 mM NH_4Cl, 12 mM $NaHCO_3$ and 0.1 mM EDTA) and incubated for 3 min on ice. Then, 5 ml FACS buffer was added, cells were resuspended and centrifuged at 370*g* for 7 min at 4 °C. Cell pellet was resuspended in FACS buffer containing purified anti-CD16/32 and 2% rat serum (liver) or 2% rat serum only (bone marrow) and incubated for 15 min at 4 °C. Samples were immune-stained with antibody mixes for 30 min at 4 °C. The complete list of antibodies used can be found in Supplementary Table 8. Data were acquired with FACSymphony A5 (BD Biosciences) or LSRII and analysed in FlowJo Software. For sorting of KCs and hepatocytes, liver cell suspension was prepared as described above with the following modifications: first, 1 ml twice-concentrated digestion mix was used for tissue digestion; second, digestion was performed at room temperature and centrifugation at 50*g* for 3 min was omitted to retain hepatocytes; and last, all steps were performed with buffers containing 1 mM of flavopiridol (F3055, Sigma-Aldrich). Cells were stained by antibody mixes and sorted using FACS ARIA III cell sorter (BD Biosciences) directly into 500 µl lysis buffer (79306, Qiagen). For KC metabolic flow cytometry assays, single-cell suspensions were blocked with anti-CD16/32 (1%) and rat serum (2%) in FACS buffer, followed by surface marker staining for 30 min at 4 °C. Cells were washed and fixed in 1% paraformaldehyde for 5 min and then permeabilized for 15 min with PBS supplemented with 0.4% Triton X-100 (X100, Sigma-Aldrich). Intracellular staining was performed for 1 h at 4 °C. Intracellular antibodies were conjugated in-house using lightning-link conjugation kits (Abcam) as previously described[26]. Cells were analysed on an ID7000 7-laser Spectral Cell Analyzer (Sony Cooperation).

Histology

For neutral lipid staining, cryo-preserved liver blocks were cut at 10 µm thickness and dried for 1 h at room temperature. Lipid staining was performed using an Oil-red-O Stain Kit (O0625, Sigma-Aldrich) according to the manufacturer's instructions. The sections were then stained with haematoxylin for 5–10 min to visualize nuclei, rinsed with distilled water and mounted with Kaiser's glycerol gelatine (pre-heated at 55 °C; 6474.1, Carl Roth). Images were taken with an Axio Lab.A1 microscope (Zeiss). For ORO staining quantification, 2–10 images of each sample

with a ×40 objective were taken and quantification was performed using QuPath software (v0.5.1). For haematoxylin and eosin (H&E) staining, paraffin-embedded liver blocks were cut at 5 µm thickness and heated for 1 h at 65 °C before staining. Sections were deparaffinized by two steps of xylol and descending series of alcohol and rinsed in distilled water. Next, sections were stained with haematoxylin solution for 1.5 min and neutralized by running tap water, followed by alcoholic eosin staining for 2 min. Sections were then dehydrated by an ascending series of alcohol and two steps of xylol and mounted with Entellan (1.07961.0100, Millipore). Images were taken with the Axio Lab.A1 microscope. Quantification of droplet adiposity in liver cells in H&E-stained histological sections was performed manually using a light microscope without the support of digital imaging or software tools. From each section, 10 random high-power fields were selected at ×10 magnification to ensure a representative selection of liver parenchyma while avoiding areas of artefacts or tissue damage. Hepatocytes were analysed for the presence of lipid droplets. All hepatocytes in each selected field were counted and classified as either normal (without lipid droplets) or lipid laden (with lipid droplets recognizable as intracellular vacuoles). The percentage of lipid-laden hepatocytes was calculated for each field by dividing the number of hepatocytes with lipid droplets by the total number of hepatocytes in the field and multiplying the result by 100. The percentages of all analysed fields were averaged to obtain a representative value for each sample. For immunofluorescence staining, cryo-preserved liver blocks were cut at 10 µm thickness, dried for 1 h at room temperature and permeabilized with PBS-T (0.4% Triton X-100; X100, Sigma-Aldrich) for 1 h at room temperature. Thereafter, tissue was blocked with PBS-T containing 2% BSA (37525, Thermo Scientific) and 2% donkey serum (D9663, Sigma-Aldrich) for 2 h at room temperature, followed by primary antibody staining overnight at 4 °C, and secondary antibodies hosted in donkey for 2 h at room temperature. Nuclei were stained with DAPI (42281, BioLegend). Immunofluorescence images were acquired with a Zeiss LSM Airyscan 880 microscope (Zeiss) and processed with Fiji[61].

Direct infusion lipidomics

Livers were isolated from ice-cold PBS-perfused mice and snap-frozen in liquid nitrogen. Ten milligrams were homogenized in ddH_2O using a Precellys homogenizer (Peqlab Biotechnology). For lipid extraction, 50 µl of the homogenate was added to 500 µl extraction mix ($CHCl_3$:MeOH 1:5 containing the following internal standards: 210 pmol phosphatidylethanolamine (PE)(31:1), 396 pmol phosphatidylcholine (PC)(31:1), 98 pmol phosphatidylserine(31:1), 84 pmol phosphatidylinositol(34:0), 56 pmol phosphatidic acid(31:1), 51 pmol phosphatidylglycerol(28:0), 28 pmol cardiolipin(56:0), 39 pmol lysophosphatidic acid(17:0), 35 pmol lysophosphatidylcholine (LPC) (17:1), 38 pmol lysophosphatidylethanolamine(17:0), 32 pmol ceramide(17:0)), 99 pmol sphingomyelin(17:0), 55 pmol glucosylceramide(12:0), 14 pmol monosialodihexosylganglioside(18:0-D3), 339 pmol triacylglycerol(50:1-d4), 111 pmol cholesteryl ester(17:1), 64 pmol diacylglycerol(31:1), 103 pmol monoacylglycerol(17:1), 724 pmol cholesterol(D6) and 45 pmol carnitine(15:0)) and subsequently sonicated for 2 min and centrifugated at 20,000*g* for 2 min. The supernatant was collected into a new tube, and 200 µl chloroform and 800 µl 1% AcOH water were added. The sample was shaken and centrifuged for 2 min at 20,000*g*. The upper aqueous phase was discarded and the lower phase was transferred into a new tube and evaporated in a speed vacuum concentrator (45 °C at 10 min). Spray buffer (500 µl of 8:5:1 2-propanol:MeOH:H_2O and 10 mM ammonium acetate) was added to the sample and sonicated for 5 min, infused at 10 µl min^{-1} into a Thermo Q Exactive Plus spectrometer equipped with the heated electrospray ionization II ion source for direct infusion lipidomics. MS1 spectra (resolution of 280,000) were recorded in 100-*m*/*z* windows from 250 to 1,200 *m*/*z* (positive) and 200 to 1,700 *m*/*z* (negative) followed by recording tandem mass spectrometry spectra (resolution of 70,000) by data-independent acquisition in 1-*m*/*z* windows from 200 to 1,200 (positive) and 200 to 1,700 (negative) *m*/*z*. Raw files were converted to .mzml files and imported into and analysed by LipidXplorer software (v1.2.8.1)[62] using custom mfql files to identify sample lipids and internal standards.

Lipidomics analysis

Raw measurements of the lipidome were quantified in relation to internal standards measured simultaneously on the same instrument. The resulting values were normalized by the amount of tissue to obtain measurements in pmol mg^{-1}. All lipid species that remained constant across all samples were removed from the dataset. In addition, species belonging to the triacylglycerol class with odd numbers of double bonds were excluded, as they were unlikely to originate from mice. This resulted in a set of 19 lipid classes: cholesteryl ester, ceramide, diacylglycerol, dihexosylceramide, hexosylceramide, LPC, ether-linked LPC, lysophosphatidylethanolamine, monoacylglycerol, phosphatidic acid, PC, ether-linked PC, PE, ether-linked PE, phosphatidylglycerol, phosphatidylserine, sphingomyelin, unsaturated fatty acyl tails of triacylglycerol (unsat) and saturated fatty acyl tails of triacylglycerol (sat). Following the selection process, the dataset consisted of 476 metabolites for C57BL/6Jrcc mice (69 dropped) and 443 metabolites for the HIF1α model (31 dropped). Within each sample, the species belonging to the same class were aggregated by calculating the mean. The results were then summarized by computing the mean per condition. Log_2 fold changes were calculated by comparing each condition to the control condition CD_MCD_LCD. For each lipid class, the conditions were assessed for significant deviations from the control condition using the lm function in R. Subsequently, a hierarchical clustering analysis was performed on the resulting dataset, both row wise and column wise, based on the Euclidean distance with complete linkage. The colour legend for the HIF1α mouse model is not evenly spaced around zero. This deviation arose from significant changes with low-effect sizes. To still indicate the direction of change, the space around zero was adjusted accordingly. The colour histogram shown represents the entire set of lipid species, not just the selected species shown in the main figure. The value of 1 was added to the data before performing the logarithmic transformation (log_2) and performing PCA.

Multiplexed cytokine and chemokine assay

The Immune Monitoring 48-Plex Mouse ProcartaPlex Panel (EPX480-20834-901, Invitrogen) was used. Of sera, 25 µl was thawed and analytes were evaluated using Luminex xMAP system. All reagents were prepared and used according to the manufacturer's instructions. Cytokines that were below the detection threshold in more than 80% of the samples were not plotted.

The values displayed within the heatmap are $log_{10} + 1$ transformed and ordered by decreasing overall mean.

Library preparation and RNA-seq

cDNA library for sequencing was prepared as described in the SMART-Seq2 protocol[63]. The mRNA was extracted and primed utilizing poly-T oligonucleotides and converted into cDNA by SMART reverse transcription. Pre-amplification was performed by SMART ISPCR, followed by fragmentation using the Nextera XT DNA Library Preparation kit (Illumina), amplification and indexing. Library fragments were then selected by size (300–400 bp) and purified using SPRIBeads (Beckman-Coulter). The Agilent high-sensitivity D5000 assay was used to measure the size distribution of cDNA libraries on a Tapestation 4200 system (Agilent). Quantifying cDNA libraries was performed using a Qubit high-sensitivity dsDNA assay (Thermo Fisher). Sequencing was performed using a 75-bp single-end setup on the NextSeq500 system (Illumina), applying NextSeq 500/550 High Output Kit (v2.5; Illumina). Library fragments were then selected by size (300–400 bp) and purified using SPRIBeads (Beckman-Coulter).

The Agilent high-sensitivity D5000 assay was used to measure the size distribution of cDNA libraries on a Tapestation 4200 system (Agilent). The cDNA libraries were quantified using a high-sensitivity dsDNA assay (Qubit). To quantify the abundances of transcripts from the bulk RNA-seq data, Kallisto pseudo alignment was applied[64].

Transcriptomics analysis

The raw transcriptome files were prepared for Kallisto import to DESeq2 using the genecode annotation M16 (https://www.gencodegenes.org/mouse/release_M16.html) to correct for library size based on the provided average transcript length. Outliers (eight from the C57BL/6Jrcc dataset and three from the *Hif1a* dataset) were identified on the basis quality assessment and filtering of low-quality samples. The set of genes was further refined to include only protein-coding genes that were non-constant across all present samples. Low-expressed genes, defined as those with less than 10 counts in 25% of the samples, were also removed. PCA was performed on the variance-stabilized counts. DESeq2 (ref. 65) analysis was conducted to identify DEGs within each cell type. The default settings in DESeq2 were used. A gene was called differentially expressed if its corresponding Benjamini–Hochberg adjusted *P* value was less than 0.1 for the tested contrast. For the KC P0 DEGs subjected to transcription factor inference analysis, the absolute LFC threshold was set to 2. The DEGs were separated into two sets based on the sign of the LFC. Each set of DEGs was subjected to an over-representation analysis to identify enriched GO terms, HALLMARK pathways and KEGG pathways using the respective functions in clusterProfiler[66]. To reduce observed redundancy in the GO terms, the 'simplify' function in clusterProfiler was used, which calculates the similarity among enriched terms based on their information content and selects a representative term with the lowest adjusted *P* value[67]. The universe for the over-representation analysis consisted of all genes used for the differential expression analysis. For the ligand–receptor analysis, DEGs with an absolute LFC greater than 2 in the KC set were subsetted to include ligands recorded in the CellTalk database[68]. For the hepatocyte dataset, all expressed genes (more than 10 counts in *Hif1a*-WT or *Hif1a*-KO HFD_MCD conditions; not necessarily differentially expressed) were subsetted to include recorded receptors within the same database. Interactions between differentially expressed ligands from KCs and expressed receptors from hepatocytes were extracted from the CellTalk database and plotted. The order of ligands was based on their LFC from lowest to highest. A co-expression network analysis using hCoCena[25] was conducted on the filtered and DESeq2 normalized counts, following the provided showcase Notebook[25]. hCoCena calculates pairwise correlations among the top most varying genes (the number needs to be user-specified) and constructs a network where vertices represent genes with at least one edge characterized by a correlation above a specified threshold. Here hCoCena was performed using the top 5,000 genes as input and all edges were kept with a correlation above 0.7. The resulting network, with 4,214 nodes and 286,853 edges, was then clustered using the Leiden algorithm[69]. Clustering was performed with 100 iterations. Each node that was advised to more than three clusters during the process was disregarded in the proceeding cluster analysis. The identified gene sets were summarized using Group Fold Change[25] for each condition and displayed on a heatmap. Each cluster set was subjected to an over-representation analysis, with the hCoCena-input genes specified as the universe for testing. Manually selected terms from GO, KEGG and HALLMARK sets are displayed for each cluster to avoid term cluttering. For selected enriched terms, their intersection with the cluster genes was recovered, namely, 'oxidative phosphorylation' with turquoise and lightgreen, 'glycolysis' and 'cell activation involved in immune response' with steelblue. The resulting set of genes was further manually reduced. The mean expression values for those intersectional genes were displayed and scaled across each condition. The columns were hierarchically clustered on the basis of the Euclidean distance with complete linkage. Transcription factor inference analysis was conducted using the CollecTRI[38] framework, which integrates information from multiple sources, including RegNetwork[70], ChEA3 (ref. 71), Pathway Commons[72] and DoRothEA[73]. Within this analysis, a linear model was used to estimate the transcription factor activity. The model predicts the value of the DEGs solely based on the interaction weights between transcription factors and their respective target genes derived from CollecTRI. The final score was the *t*-value of the slope of the fitted model. A positive value indicates an active transcription factor. This analysis was conducted using decoupler's[74] functionality.

snRNA–ATAC-seq

Nuclei were isolated from approximately 50 mg of snap-frozen adult liver tissue to enable simultaneous snRNA-seq and snATAC-seq, capturing both transcriptional profiles and chromatin accessibility. Nuclei were prepared using the Chromium Next GEM Single Cell Multiome ATAC + Gene Expression Kit (1000283, 10X Genomics). In detail, snap-frozen liver tissue was first cut on dry-ice into small pieces and homogenized with a pestle in homogenization buffer containing 320 mM sucrose, 5 mM $CaCl_2$, 3 mM Mg-acetate, 10 mM Tris, 0.1 mM EDTA, 0.1% IGEPAL CA-630 (Sigma), 0.1 mM phenylmethylsulfonyl fluoride (Sigma), 0.2 U μl^{-1} RNase inhibitor (New England Biolabs), 1 mM flavopiridol and 1 mM β-mercaptoethanol (ITW Reagents) in nuclease-free water. Homogenate was then passed through a 70-μM cell strainer and mixed with equal volume of gradient medium containing 50% OptiPrep (StemCell Technologies), 5 mM $CaCl_2$, 3 mM Mg-acetate, 10 mM Tris-HCl (pH 8), 0.1 mM phenylmethylsulfonyl fluoride (Sigma) and 1 mM β-mercaptoethanol (ITW Reagents) in nuclease-free water. Diluted homogenate was slowly laid atop a cushion (75% of the volume of diluted homogenate) containing 29% OptiPrep, 77.5 mM KCl, 15.5 mM $MgCl_2$, 31 mM Tris-HCl (pH 8) and 129.2 mM sucrose in UltraPure H_2O and centrifuged with low acceleration and maximum deceleration at 10,000*g* at 4 °C for 30 min. The pellet containing nuclei was resuspended in 1X PBS containing 1% BSA, 0.2 U μl^{-1} RNase inhibitor (New England Biolabs) and 1 mM flavopiridol, stained with 7-AAD and purified by fluorescence-activated cell sorting using FACS ARIA III (BD Biosciences) for high-quality, monoploid and 7-AAD nuclei. For nuclei permeabilization, approximately 500,000 sorted nuclei were incubated for 2 min in a 0.1× lysis buffer (10 mM Tris-HCl (pH 7.4), 10 mM NaCl, 3 mM $MgCl_2$, 0.1% IGEPAL CA-630, 0.1% Tween-20, 0.01% digitonin, 1 mM dithiothreitol, 1% BSA and 1 U μl^{-1} RNase inhibitor, with 1 μM flavopiridol in nuclease-free water). Following permeabilization and washing steps, nuclei concentration was adjusted to 5,000 nuclei per microlitre in ice-cold 1× nuclei buffer (2000153/2000207, 10X Genomics) and were incubated in a transposition mix containing a transposase, allowing adapter sequences to be added to the ends of DNA fragments. Furthermore, 16,000 nuclei were used for analysis with the Next GEM Single Cell Multiome ATAC + Gene Expression Kit (PN-1000230, 10X Genomics) and Gel Beads in Emulsion (GEMs) using the Chromium Next GEM Chip J Single Cell Kit. After GEM reverse transcription (GEM-RT) cleanup, pre-amplification of the sample was performed, producing material for both ATAC library construction and cDNA amplification for gene expression library construction. During the reverse transcription reaction, cDNA tagging was achieved with 16-nucleotide barcodes and 10-nucleotide molecular identifiers. The pre-amplified product was split into two aliquots: 40 μl for ATAC library construction and 35 μl for further cDNA amplification. For snRNA-seq library preparation, 25% of the total cDNA was used to generate gene expression (GEX) libraries. Libraries were prepared and sequenced according to the manufacturer's protocols: snATAC libraries used the 10X Genomics Single Index N Set, and snRNA-seq libraries used the Dual Index TT Set A. Pooled and barcoded libraries were sequenced on an Illumina NextSeq 2000 system with P3 flow cells, achieving an average depth of 30,000 reads per nucleus for both snRNA-seq and snATAC-seq libraries. The sequencing quality was assessed using FastQC (v0.12.1) executed within a containerized environment provided by biocontainers

using Podman. All files passed initial quality assessment. Following assessment, Cell Ranger ARC (v2.0.0; 10X Genomics) was used for simultaneous alignment and quantification of both modalities. The cellranger-arc count pipeline was run according to the manufacturer's instructions using the 10X Genomics-provided reference dataset refdata-cellranger-arc-mm10-2020-A-2.0.0, which is based on the mm10 genome assembly and including introns. The automatically obtained quality assessment alerted for both conditions that the amount of valid ATAC barcodes was at 54% (ideally more than 80%). Despite the low proportion, both datasets were used because other critical ATAC quality metrics, such as fragment count and enrichment scores, met acceptable thresholds. Single-cell RNA-seq and ATAC-seq data were processed using mainly the Seurat and Signac packages in R. Both modalities were extracted from the 10X Genomics 'filtered feature matrix file', in which count data were used for additional filtering of low-quality cells, before using MACS3 to perform the peak calling within the remaining cells to reduce computational time. Applied thresholds were: cells with RNA counts below 500, number of genes less than 200 or more than 2,500, and mitochondrial RNA content above 1% (as for single-nucleus sequencing, we expected none). Resulting peaks were also used for filtering of low-quality cells. Applied thresholds were: ATAC counts below 1,000, nucleosome signal more than 2 and transcription start site enrichment less than 1. In addition, peaks were removed that overlapped with non-standard chromosomes: genomic blacklist regions. The preprocessing led to 8,197 total cells for CD_MCD_LCD and 5,017 cells for HFD_MCD_LCD. Each RNA-seq dataset was pre-processed within each condition before integration using SCTransform, regressing out the percentage of mitochondrial DNA. The integration of RNA and ATAC data across conditions followed the outline from Kim et al.[75]. Accordingly, RNA data integration began with the selection of 3,000 integration features using SelectIntegrationFeatures in Seurat. The datasets were prepared for integration with PrepSCTIntegration, and integration anchors were identified using FindIntegrationAnchors with SCTransform (SCT) normalization. The anchors were then used to integrate the datasets across conditions via IntegrateData. ATAC count integration started by creating a feature matrix for each condition based on a unified peak set that was shared across conditions. Dimensionality reduction for ATAC data relied on latent semantic indexing, which included feature selection of most variable peaks, transformation of peak counts and singular value decomposition. To improve the integration, Harmony was applied (RunHarmony). Harmony aligns datasets by projecting them into a shared low-dimensional space while minimizing the effects of batch-specific biases. For the final integration across modalities, multimodal neighbours were identified by combining RNA-based PCA and ATAC-based Harmony embeddings (FindMultiModalNeighbors) across 50 dimensions for each modality, without the first dimension for Harmony, as commonly done, aiming for additional batch correction. Clusters were identified using the weighted nearest neighbour similarity graph (FindClusters) with a resolution of 0.5. This approach allowed the simultaneous integration of RNA and ATAC data for both conditions while leveraging the complementary information from both modalities. Cluster-specific marker genes were identified by calculating differential expression for each cluster using FindAllMarkers in Seurat. Markers were filtered based on minimum expression percentage (0.10), minimum differential expression percentage (0.20) and log fold-change threshold (0.20), retaining only positive markers. Cell-type annotation was based on the expression of a curated gene set within the identified markers. Subclustering was performed on the cells annotated as KCs from the integrated dataset. Again, multimodal neighbours were identified (FindMultiModalNeighbors) using PCA for RNA and Harmony for ATAC, followed by UMAP for dimensionality reduction (RunUMAP) and clustering (FindClusters), as done for the dataset using all cell types. Subclusters with fewer than 50 cells were excluded due to low numbers, and markers for each remaining cluster were characterized using the FindAllMarkers function in Seurat with the number of neighbours set to 60. Subcluster characterization was based on the expression of a curated gene set within the identified markers. To analyse intercellular communication involving the differing KC subclusters to hepatocytes, a CellChat analysis was performed. The analysis followed CellChat instructions for comparisons and analysis of multiple datasets. Normalized RNA expression data were used to define communication networks between KC subclusters and other cell populations. Overexpressed genes and interactions were identified for each condition, identifying 1,366 (CD_MCD_LCD) and 1,458 (HFD_MCD_LCD) highly variable ligand–receptor pairs subsequently used for signalling inference. Communication probabilities were computed using the 10% truncated mean for calculating the gene expression per cell group. Interactions with fewer than ten participating cells were filtered out to ensure robustness. The KC-specific communication networks were compared across conditions using rankNet function. A paired Wilcoxon test was performed to determine whether there was a significant difference of the signalling information flow between two conditions. Potential activated transcription factors were investigated using the package decouplR. For the analysis, the transformed RNA-count data were subsetted to the union of DEGs between the KC subclusters. The resulting set was subjected to the unified linear model to identify potential regulators (transcription factors). Only regulators were tested, which had at least ten known targets among the union differentially expressed set. According to decouplR's vignette, the resulting score matrix, representing regulations strength, was scaled and centred. The 25% trimmed mean activity per cluster for each condition is displayed to provide a robust central tendency measure.

Metabolomics analysis

Metabolomics analysis was conducted using data obtained from Metabolon. The Metabolon platform performed preprocessing steps on the data, including imputation of missing values and natural log transformation. In summary, the raw peak area data were median scaled per metabolite and then normalized by the value of the extracted volume. It was further rescaled to have a median equal to 1. Missing values for each metabolite were imputed with the minimum value observed across all samples. Finally, a natural logarithm transformation was applied to the metabolomic data, as it typically exhibited a log-normal distribution. For the PCA, the data were subjected to batch correction based on the day of the experiment, which was identified as a significant source of variance in the initial PCA analysis. The identified effect was treated as a batch factor in the ComBat function of the sva package[76] for batch correction. The corrected data were then used for PCA analysis. To identify metabolites with significant effects of diet, genotypes or their interaction on their respective levels, an ANOVA was performed. Specifically, a contrast[77] was applied within the ANOVA to compare metabolite levels between maternal obese (HFD_MCD_LCD) and maternal lean (CD_MCD_LCD) conditions. The resulting set of 129 metabolites with significant raw *P* values was further analysed using Metaboanalyst (https://www.metaboanalyst.ca/)[78] for pathway over-representation analysis. The HMDB IDs provided by Metabolon were used as input, resulting in a reduction to 111 metabolites due to missing labels. Furthermore, mapping to Metaboanalyst failed for ten additional metabolites. Default parameters were used for all remaining settings, except for choosing *Mus musculus* (KEGG) as the pathway library and applying out-degree centrality as the topology analysis method.

Hepatocyte and KC isolation for ex vivo experiments

Eight-to-ten-week-old chow diet-fed C57BL/6JRcc female mice were used to isolate hepatocytes. Therefore, a two-step collagenase liver perfusion was performed. First, 7 min after injecting heparin-sodium (Ratiopharm; 30 units per gram body weight), mice were anaesthetized with ketamine–xylazine. Next, a 26 G indwelling venous catheter (0.62 mm × 19 mm; 391379, BD Neoflon Pro) was inserted into the portal

vein. Perfusion was initiated with 25 ml Hank's balanced salt solution containing 0.5 mM EGTA (pH 7.4) at a rate of 2.5 ml min^{-1} using a peristaltic pump, and subsequently with 25 ml collagenase buffer (William's Medium E, P04-29510, Pan-Biotech) supplemented with 3.6 mM $CaCl_2$, 0.1 U ml^{-1} collagenase NB46 (17465, Serva Electrophoresis) and 10 mM HEPES at 37 °C at a rate of 1.25 ml min^{-1}. Liver cells were released by gentle swirling with forceps into 40 ml suspension medium (William's Medium E supplemented with 10% FCS, 2 mM L-glutamine, 100 units per millilitre penicillin and 100 µg ml^{-1} streptomycin). Hepatocytes were pelleted at 50*g* for 3 min at room temperature. The pellet containing the hepatocytes was resuspended in fresh suspension medium and plated on collagen-coated 24-well plates for co-culture experiments with KCs at a density of 30,000 cells per well or on collagen-coated 96-well plates for factor screening experiments at a density of 5,000 cells per well. To ensure a viable hepatocyte culture, cells were pre-incubated for 3 h at 37 °C and 5% CO_2 to allow for attachment. Thereafter, the medium was replaced with fresh suspension medium containing LD540 (0.02 µg ml^{-1}) and vitamin C (1 µg ml^{-1}) for live-cell imaging using the IncuCyte SX5 (Sartorius). To isolate KCs, 11–15-week-old mice were perfused with the same method as isolating hepatocytes but without the in vivo digestion step. After perfusion, liver was minced and digested in a digestion mix (PBS containing 1 mg ml^{-1} collagenase D, 100 U ml^{-1} DNase I, 2.4 mg ml^{-1} dispase and 3% FCS) for 30 min at 37 °C without agitation. Digested liver was further disrupted with gentle pipetting, filtered through a 100-µm cell strainer and centrifuged at 400*g* for 10 min at 4 °C. Pellet was washed with ice-cold FACS buffer (PBS containing 0.5% BSA and 2 mM EDTA) and centrifuged at 50*g* for 3 min at 4 °C to remove hepatocytes. The supernatant was then further filtered and washed with FACS buffer to obtain a clean, single-cell suspension and centrifuged at 400*g* for 10 min at 4 °C. The resulting pellet was then blocked with 1% anti-mouse CD16/32 (101302, BioLegend) and 5% rat serum (C13SDZ, Bio-Rad) for 10 min at 4 °C followed by incubation with biotinylated CD11b antibody (101204, BioLegend) for 30 min at 4 °C. Cells were then washed, incubated with pre-washed streptavidin-conjugated magnetic beads (480016, BioLegend), washed and enriched in a 12-well untreated cell-culture dish mounted atop a magnet. Enriched cells were abundantly washed in FACS buffer and subsequently counted using a Neubauer chamber. Cells (3×10^5) were plated onto a 13-mm diameter, untreated glass coverslip (VWR; co-culture experiments) or 2–4×10^6 cells onto an untreated glass slide (Fisher Scientific; proteomics experiments). Cells were attached for 2 h in macrophage medium (DMEM, containing 1% penicillin–streptomycin, 10% FBS and 1 mM sodium pyruvate) in a cell culture incubator at 37 °C with 5% CO_2. After attachment, cells were abundantly washed with PBS. Macrophages on coverslips were used for co-culture experiments as described below. Macrophages for proteomics experiments were scraped off in PBS, centrifuged at 400*g* at 4 °C for 5 min to obtain pellets, snap-frozen in liquid nitrogen and further processed for proteomics as described below.

Live-cell imaging for hepatocyte culture experiments and data analysis

For hepatocyte–KC co-culture experiments, a plastic ring (8 mm in height × 15 mm in diameter) was placed in each well of hepatocytes seeded as described above. A glass coverslip attached with approximately 3×10^4 KCs (resulted from initially seeded 3×10^5 CD11b magnet-enriched cells), isolated from either CD_MCD_LCD or HFD_MCD_LCD mice, was positioned upside-down on the plastic ring. LD540 was then added, and signal was recorded by live imaging hourly for 4 h in the IncuCyte SX5, with each mouse represented by multiple replicates and nine fields of view (FOVs) per well. For treatment of hepatocytes with APOE or APOA1, APOE (1 µg ml^{-1} recombinant mouse APOE; ab226314, Abcam) or APOA1 (2 µg ml^{-1} recombinant mouse APOA1; 50918-M08H, Sino Biological) was pre-incubated with hepatocyte medium at 37 °C for 30 min. The pre-incubated medium was then added to hepatocytes already containing 1 volume of hepatocyte medium. TNF (0.1 µg ml^{-1} recombinant mouse TNF; 130-101-688, Miltenyi)-treated hepatocytes were used as positive controls. Non-treated hepatocytes served as negative controls. For each mouse, three replicates were prepared, LD540 was then added and the signal was recorded by live imaging hourly for 4 h in the IncuCyte SX5, with four FOVs imaged per well. The LD540-integrated intensity was quantified by multiplying μm^2 per FOV using the IncuCyte SX5 analysis software. A cell area filter was applied to ensure single-cell detection. Out-of-focus FOVs were excluded from analysis, as indicated by red labelling in the raw data spreadsheet. For co-culture data, the mean integrated LD540 signal per mouse was calculated following outlier removal by the interquartile range method. Statistical tests included the Shapiro–Wilk test for normality, Levene's test for variance homogeneity, and two-sample *t*-tests to compare CD versus HFD conditions at each time point. For screening data, mean LD540 measurements were averaged across replicates and normalized to the control measurement mean for each mouse after 3 h and 4 h in the co-culture experiment, and after 2 h in the screening assay.

KC proteomics analysis

KCs were isolated and pelleted as described above. Pelleted cells were thawed and lysed in urea lysis buffer (8 M urea and 50 mM Tris (pH8)), DNA was sheared with 28 U ml^{-1} benzonase (Sigma), and disulfide bridges were reduced and alkylated with 10 mM Bond-Breaker TCEP solution (Thermo) and 30 mM chloroacetamide. Non-dissolved cellular debris was removed by centrifugation at 15,000*g* for 10 min, and clean supernatants were transferred to fresh tubes. Protein concentrations were determined with the Pierce 660 nm Protein-Assay-kit (Thermo). Of protein input, 25 µg was used for digestion in 2 M urea (diluted with 50 mM Tris (pH 8)) with a trypsin–LysC mixture (1:50 (enzyme:protein)) at 800 rpm for 16 h. Protein digestion was stopped with 1% formic acid, peptides were desalted on in-house-produced SDB-RPS Stage Tips and loaded onto EvoTip Pure trap columns following the manufacturers' protocol.

A liquid chromatography–tandem mass spectrometry system consisting of an Evosep One liquid chromatograph (Evosep) and a timsTOF Pro 2 mass spectrometer (Bruker) was used for peptide separation and acquisition. Reversed-phase separation was performed on an Aurora Elite analytical column (IonOpticks) using the 40 samples-per-day separation method with a 31-min gradient preprogrammed on the liquid chromatography system. Eluting peptides were on-line transferred into the mass spectrometry via a CaptiveSpray ionisation source operated at a constant voltage of 1.5 kV. We used the data-independent acquisition parallel accumulation-serial fragmentation mode with the TIMS analyser operating with 100-ms accumulation and ramping times and a 100% duty cycle. Peptide ranges were limited to a mass-to-charge range of 350–1,100 m/z and an ion mobility range of 0.63–1.45 Vs cm^{-2} with 12 pydiAID-optimized data-independent acquisition parallel accumulation-serial fragmentation windows of variable widths[79]. We increased collisional energies stepwise from 24 eV at 0.70 Vs cm^{-2} and 49 eV at 1.35 Vs cm^{-2} for peptide fragmentation. The mass spectrometry proteomics data have been deposited to the ProteomeXchange Consortium via the PRIDE partner repository[80] with the dataset identifier PXD058285. Spectral library prediction, peptide identification and protein quantification were performed in library-free mode using DIA-NN (v1.8.1)[81]. The SwissProt *Mus musculus* database was used for predicted spectral library (downloaded from UniProt: 2022-12-28). In silico digestion was set to trypsin as the digestion enzyme with a maximal one miss-cleavage and cysteine carbamidomethylation set as fixed modifications. Precursor peptides were filtered at a false discovery rate (FDR) < 1%. The match-between-runs option was enabled. Using the DIA-NN main output table, we performed protein group intensity normalizations with the MaxLFQ algorithm[82] implemented in the DIA-NN R-package. Only proteotypic peptides were considered

for quantification. Statistical analysis was performed in the Perseus software suite (v1.6.15)[83]. Protein group label-free quantification intensities were $\log_2$ transformed and filtered for protein groups with data completeness in at least one condition. Missing values were replaced by random value drawing from 1.8 standard deviations downshifted and 0.3 standard deviations broad normal distributions. Significantly regulated proteins between any conditions were identified by ANOVA multiple-sample testing (S0 = 0.5, FDR < 0.1 with 250 randomizations) and all proteins were *z*-score normalized. For visualization, the dataset was summarized by taking the mean over all samples per group, namely, WT and KO in maternal lean, as well as WT and KO in maternal obese. The summarized data were objected to *k*-means clustering using $k = 6$ to obtain groups of proteins with varying expression patterns across samples from which several interesting representatives were chosen to be highlighted.

Statistics and bioinformatic tools

Statistical assessment was performed with one-way ANOVA with Tukey's multiple comparisons method, the Kruskal–Wallis test, the unpaired Student's *t*-test, the Mann–Whitney test or the Wilcoxon rank sum test, depending on the dataset, and following an assessment of normality. R-studio and Prism were used for the statistical evaluation and visualization. Statistical significance was represented via the probability (*P* value) as follows: not significant (NS) > 0.05, $^{*}P < 0.05$, $^{**}P < 0.01$ and $^{***}P < 0.001$. All bar graphs represent mean values. In all of the aforementioned analyses, PCA was performed using the prcomp function in R on centred data. Significance levels were consistently set at $P < 0.05$. Raw *P* values were adjusted for multiple testing using the false discovery rate method and considered significant if the adjusted $P < 0.1$. The analysis was implemented using R (v4.2.0)[84] and Bioconductor (v3.15)[85]. Detailed information about every package used, including all dependencies, along with their respective versions, can be found in the renv.lock file located in the GitHub repository (https://github.com/LeaSeep/MaternalObesity) generated with the renv package[86]. The main analysis and visualization packages used can be found in Supplementary Table 9 that contains all references. All scripts, as well as the necessary data files, are available in the GitHub repository to reproduce all the results presented in the article, including additional results, by running the respective main files or provided RMarkdown Documents for the hCoCena. Furthermore, a database file has been provided, which presents all the statistical figures and serves as a comprehensive resource for quick reference and independent verification of our own hypothesis or results. These resources have been made available to facilitate reproducibility and enable researchers to conduct their own investigations with ease. A snapshot of the GitHub repository can be found on Zenodo[87] (https://doi.org/10.5281/zenodo.14287647).

Reporting summary

Further information on research design is available in the Nature Portfolio Reporting Summary linked to this article.

Data availability

The raw transcriptome files and the count data have been deposited in NCBI's Gene Expression Omnibus (GEO)[88] and are accessible through GEO Series accession number GSE237408 (https://www.ncbi.nlm.nih.gov/geo/query/acc.cgi?acc=GSE237408). Raw and processed lipidomics data are available at Metabolomics Workbench[89] where it has been assigned study IDs ST002781 and ST002782 within the project PR001715. The Metabolome data are available at Metabolomics Workbench[89] where it has been assigned with the study ID ST002754 within the same project as the lipidomics data (https://doi.org/10.21228/M81D9R). All imaging data used for quantification are available at Bonndata (https://doi.org/10.60507/FK2/PP2MPB). Source data are provided with this paper.

56. Maeda, K. et al. Wnt5a–Ror2 signaling between osteoblast-lineage cells and osteoclast precursors enhances osteoclastogenesis. *Nat. Med.* **18**, 405–412 (2012).
57. Srinivas, S. et al. Cre reporter strains produced by targeted insertion of EYFP and ECFP into the ROSA26 locus. *BMC Dev. Biol.* **1**, 4 (2001).
58. Daigle, T. L. et al. A suite of transgenic driver and reporter mouse lines with enhanced brain-cell-type targeting and functionality. *Cell* **174**, 465–480.e22 (2018).
59. Ryan, H. E. et al. Hypoxia-inducible factor-1α is a positive factor in solid tumor growth. *Cancer Res.* **60**, 4010–4015 (2000).
60. Matthews, D. R. et al. Homeostasis model assessment: insulin resistance and β-cell function from fasting plasma glucose and insulin concentrations in man. *Diabetologia* **28**, 412–419 (1985).
61. Schindelin, J. et al. Fiji: an open-source platform for biological-image analysis. *Nat. Methods* **9**, 676–682 (2012).
62. Hoffmann, N., Ackerman, M. J., Machot, A. F., Schwudke, D. & Shevchenko, A. LipidXplorer 1.2.8.1. *Zenodo* https://doi.org/10.5281/ZENODO.3570469 (2019).
63. Picelli, S. et al. Smart-seq2 for sensitive full-length transcriptome profiling in single cells. *Nat. Methods* **10**, 1096–1098 (2013).
64. Bray, N. L., Pimentel, H., Melsted, P. & Pachter, L. Near-optimal probabilistic RNA-seq quantification. *Nat. Biotechnol.* **34**, 525–527 (2016).
65. Love, M. I., Huber, W. & Anders, S. Moderated estimation of fold change and dispersion for RNA-seq data with DESeq2. *Genome Biol.* **15**, 550 (2014).
66. Wu, T. et al. clusterProfiler 4.0: a universal enrichment tool for interpreting omics data. *Innovation* **2**, 100141 (2021).
67. Lord, P. W., Stevens, R. D., Brass, A. & Goble, C. A. Investigating semantic similarity measures across the Gene Ontology: the relationship between sequence and annotation. *Bioinformatics* **19**, 1275–1283 (2003).
68. Shao, X. et al. CellTalkDB: a manually curated database of ligand–receptor interactions in humans and mice. *Brief. Bioinform.* **22**, bbaa269 (2021).
69. Traag, V. A., Waltman, L. & van Eck, N. J. From Louvain to Leiden: guaranteeing well-connected communities. *Sci. Rep.* **9**, 5233 (2019).
70. Liu, Z. P., Wu, C., Miao, H. & Wu, H. RegNetwork: an integrated database of transcriptional and post-transcriptional regulatory networks in human and mouse. *Database* **2015**, bav095 (2015).
71. Keenan, A. B. et al. ChEA3: transcription factor enrichment analysis by orthogonal omics integration. *Nucleic Acids Res.* **47**, W212–W224 (2019).
72. Rodchenkov, I. et al. Pathway Commons 2019 update: integration, analysis and exploration of pathway data. *Nucleic Acids Res.* **48**, 489–497 (2019).
73. Garcia-Alonso, L., Holland, C. H., Ibrahim, M. M., Turei, D. & Saez-Rodriguez, J. Benchmark and integration of resources for the estimation of human transcription factor activities. *Genome Res.* **29**, 1363–1375 (2019).
74. Badia-I-Mompel, P. et al. decoupleR: ensemble of computational methods to infer biological activities from omics data. *Bioinform. Adv.* **2**, vbac016 (2022).
75. Kim, Y. I. L., O'Rourke, R. & Sagerström, C. G. scMultiome analysis identifies embryonic hindbrain progenitors with mixed rhombomere identities. *eLife* **12**, e87772 (2023).
76. Leek, J. T., Johnson, W. E., Parker, H. S., Jaffe, A. E. & Storey, J. D. The SVA package for removing batch effects and other unwanted variation in high-throughput experiments. *Bioinformatics* **28**, 882–883 (2012).
77. O'Callaghan, A., Kuhn, M., Weston, S., Wing, J., Forester, J. & Thaler, T. contrast: A collection of contrast methods. *CRAN* https://CRAN.R-project.org/package=contrast (2021).
78. Lu, Y., Pang, Z. & Xia, J. Comprehensive investigation of pathway enrichment methods for functional interpretation of LC–MS global metabolomics data. *Brief. Bioinform.* **24**, bbac553 (2023).
79. Skowronek, P. et al. Rapid and in-depth coverage of the (phospho-)proteome with deep libraries and optimal window design for dia-PASEF. *Mol. Cell. Proteomics* **21**, 100279 (2022).
80. Perez-Riverol, Y. et al. The PRIDE database resources in 2022: a hub for mass spectrometry-based proteomics evidences. *Nucleic Acids Res.* **50**, D543–D552 (2022).
81. Demichev, V., Messner, C. B., Vernardis, S. I., Lilley, K. S. & Ralser, M. DIA-NN: neural networks and interference correction enable deep proteome coverage in high throughput. *Nat. Methods* **17**, 41–44 (2020).
82. Cox, J. et al. Accurate proteome-wide label-free quantification by delayed normalization and maximal peptide ratio extraction, termed MaxLFQ. *Mol. Cell. Proteomics* **13**, 2513 (2014).
83. Tyanova, S. et al. The Perseus computational platform for comprehensive analysis of (prote)omics data. *Nat. Methods* **13**, 731–740 (2016).
84. R Core Team. *R: A Language and Environment for Statistical Computing*. https://www.R-project.org/ (R Foundation for Statistical Computing, 2022).
85. Huber, W. et al. Orchestrating high-throughput genomic analysis with Bioconductor. *Nat. Methods* **12**, 115–121 (2015).
86. Ushey, K. renv: Project environments. *CRAN* https://CRAN.R-project.org/package=renv (2022).
87. Seep, L. Bioinformatic analysis for developmental programming of Kupffer cells by maternal obesity causes fatty liver disease in the offspring (2.0.0). *Zenodo* https://doi.org/10.5281/zenodo.14287647 (2024).
88. Edgar, R., Domrachev, M. & Lash, A. E. Gene Expression Omnibus: NCBI gene expression and hybridization array data repository. *Nucleic Acids Res.* **30**, 207–210 (2002).
89. Sud, M. et al. Metabolomics Workbench: an international repository for metabolomics data and metadata, metabolite standards, protocols, tutorials and training, and analysis tools. *Nucleic Acids Res.* **44**, D463–D470 (2015).

Acknowledgements We thank C. Cygon, P. Kern and J. Rollheiser for their support in the laboratory; and Y. Kobayashi for providing the *Tnfrsf11a*^{Cre} mice. The work in the laboratories was supported by the following grants: funded by the Deutsche Forschungsgemeinschaft (DFG; German Research Foundation) under Germany's Excellence Strategy-EXC2151-390873048 (to E.M., J.L.S., M.D.B., C.T., J.H., D.W. and F.M.), SFB1454 (project number 432325352 to E.M., J.L.S., M.D.B., J.H., C.T., D.W., S.G., L.S. and F.M.), GRK1873/2 (to N.M. and E.M.), SFB/TRR83 28N (project number 112927078 to N.R.B. and D.W.), GRK2168 (project number 272482170 to K.M., E.M. and M.D.B.), FOR5547 (project-ID 503306912 to E.M., D.W. and K.A.) and TRR333/1 (project-ID 450149205 to D.W.); the European Research Council under the European Union's

Horizon 2020 research and innovation program (grant agreement no. 851257 to E.M.); the Jürgen Manchot Fellowship (to E.F.T.); the PhD fellowship from Boehringer Ingelheim Fonds (to K.M.); and the EMBO fellowship (ATLF 873-2023 to M.F.V.). The Metabolomics Workbench used to deposit metabolomic and lipidomics data is supported by US National Institutes of Health (NIH) grants U2C-DK119886 and OT2-OD030544. L.K. acknowledges support from MicroONE, a COMET Modul (CBmed GmbH) funded by BMK, BMDW, Styria, Vienna, and managed by FFG within the COMET program. The Austrian Federal Ministry of Science, Research and Economy, the National Foundation for Research, Technology and Development, the Christian Doppler Research Association, Siemens Healthineers, EU Horizon 2020 Marie Sklodowska-Curie Doctoral Network grants FANTOM (P101072735) and eRaDicate (101119427), the Christian-Doppler Lab for Applied Metabolomics, the Austrian Science Fund (P26011, P29251, P34781 and IPPTO doc.funds) and the Vienna Science and Technology Fund (LS19-018) provided additional support to L.K. L.K. is a member of the European Research Initiative for ALK-Related Malignancies (www.erialcl.net). This work was supported by the Open Access Publication Fund of the University of Bonn. We thank the Flow Cytometry Core Facility of the Mathematical and Natural Sciences Faculty and Flow the Cytometry Core Facility Medical Faculty at the University of Bonn for providing support and instrumentation funded by the DFG (German Research Foundation) — project numbers 341039622, 144734146, 471514137 and 01EO2107 (BMBF).

Author contributions H.H. and I.S. performed the experiments, analysed data, created the figures and wrote the manuscript. N.R.B. performed the experiments, analysed data and created the figures. N.B.-S., M.F.V., E.F.T., K.A., F.P., N.M., S.B., K.M., C.R., A.H.K. and M.J. helped with experimental procedures and analyses, as well as production of mouse cohorts. L.S. performed the bioinformatic analyses and wrote the manuscript. S.G. and J.H. supported the bioinformatic analyses. J.Z., K.W., M.H.Y. and C.T. supported the lipidomics and ex vivo hepatocyte culture analyses. D.F. and F.M. performed and analysed the proteomics experiments. L.K. performed the pathological scoring. T.U., J.L.S. and M.D.B. supported the RNA-seq experiments. M.D.B. provided the *LysM*^{Cre};*Hif1a*$^{f/f}$ mice. Z.L. and F.G. provided the *Ms4a3*^{FlpO} mice. C.L.S. and M.G. provided the *Clec4*^{DTR} mice. D.W. provided funding. E.M. conceptualized the study, analysed the data, created the figures, wrote the manuscript and provided funding. All authors contributed to and reviewed the manuscript.

Competing interests The authors declare no competing interests.

Additional information

Supplementary information The online version contains supplementary material available at https://doi.org/10.1038/s41586-025-09190-w.

Correspondence and requests for materials should be addressed to Elvira Mass.

Peer review information *Nature* thanks Rodrigo Carlessi, Janina Tirnitz-Parker and the other, anonymous, reviewer(s) for their contribution to the peer review of this work. Peer reviewer reports are available.

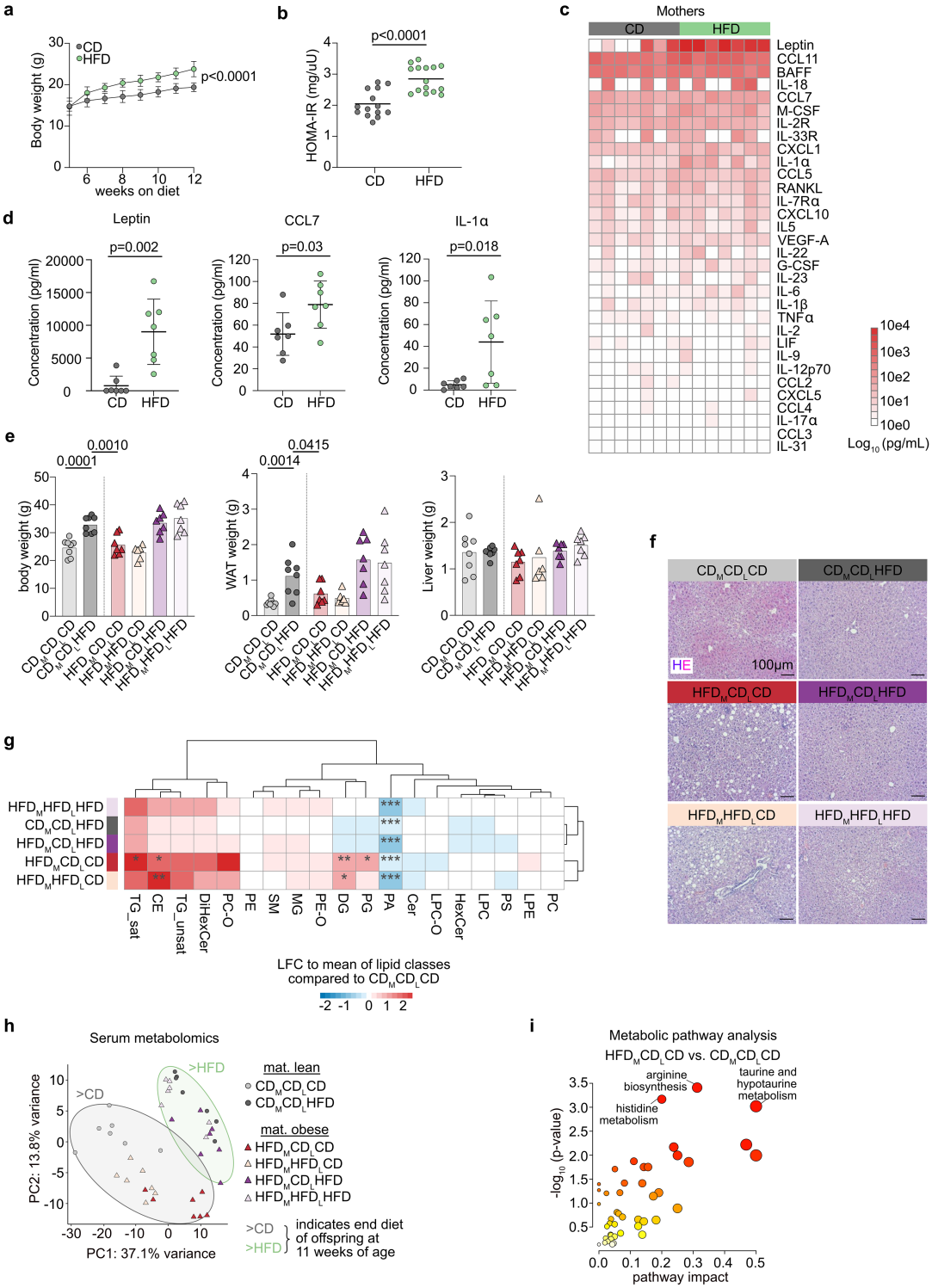

Extended Data Fig. 1 | Maternal obesity model and characterization of liver metabolic status in the offspring. a, Body weight of mothers on control diet (CD, grey) or high-fat diet (HFD, green). n = 15 mice/group. Mean ± SD is shown. Two-tailed unpaired Student's t-test. **b**, Homeostatic Model Assessment for Insulin Resistance (HOMA-IR) of mothers on CD or HFD performed after 8 weeks on respective diet. n = 15 mice/group. Mean is indicated. Two-tailed unpaired Student's t-test. **c**, Heatmap showing log-transformed values of detected cytokines and chemokines in the sera of mothers on CD and HFD. Each column represents one mouse. n = 7 mice/group. Two-tailed unpaired Student's t-test on the individual coefficients after linear fitting model and multiple testing correction using false discovery rate <0.05. **d**, Plots of results from **c** that show significance when using two-tailed unpaired Student's t-test. Mean ± SD. **e**, Body, white adipose tissue (WAT) and liver weights of offspring at 11 weeks of age. n = 8, 8, 7, 6, 7, 7 mice for CD_MCD_LCD, CD_MCD_LHFD, HFD_MCD_LCD, HFD_MHFD_LCD, HFD_MCD_LHFD, HFD_MHFD_LHFD groups, respectively, on 11 experimental days. Bar graphs show the means. **f**, Hematoxilin-eosin (HE) staining of liver sections of the offspring. Scale bars, 100 µm. Representative pictures for the mice in **e**. **g**, Heatmap of liver lipidomics in Fig. 1d showing the condition-wise Log-Fold changes (LFC) against the CD_MCD_LCD of selected lipid groups. Two-tailed unpaired Student's t-test on the individual coefficients after linear fitting model and multiple testing correction using false discovery rate <0.05 (* = p < 0.05, ** = p < 0.01, *** = p < 0.001). **h**, Metabolomics of serum from all experimental groups visualized by PCA. **i**, Enriched metabolic pathways in HFD_MCD_LCD compared to CD_MCD_LCD based on serum metabolomics data. **h, i**, *n* = 7 mice/group. One-way ANOVA – Tukey's multiple comparison test.

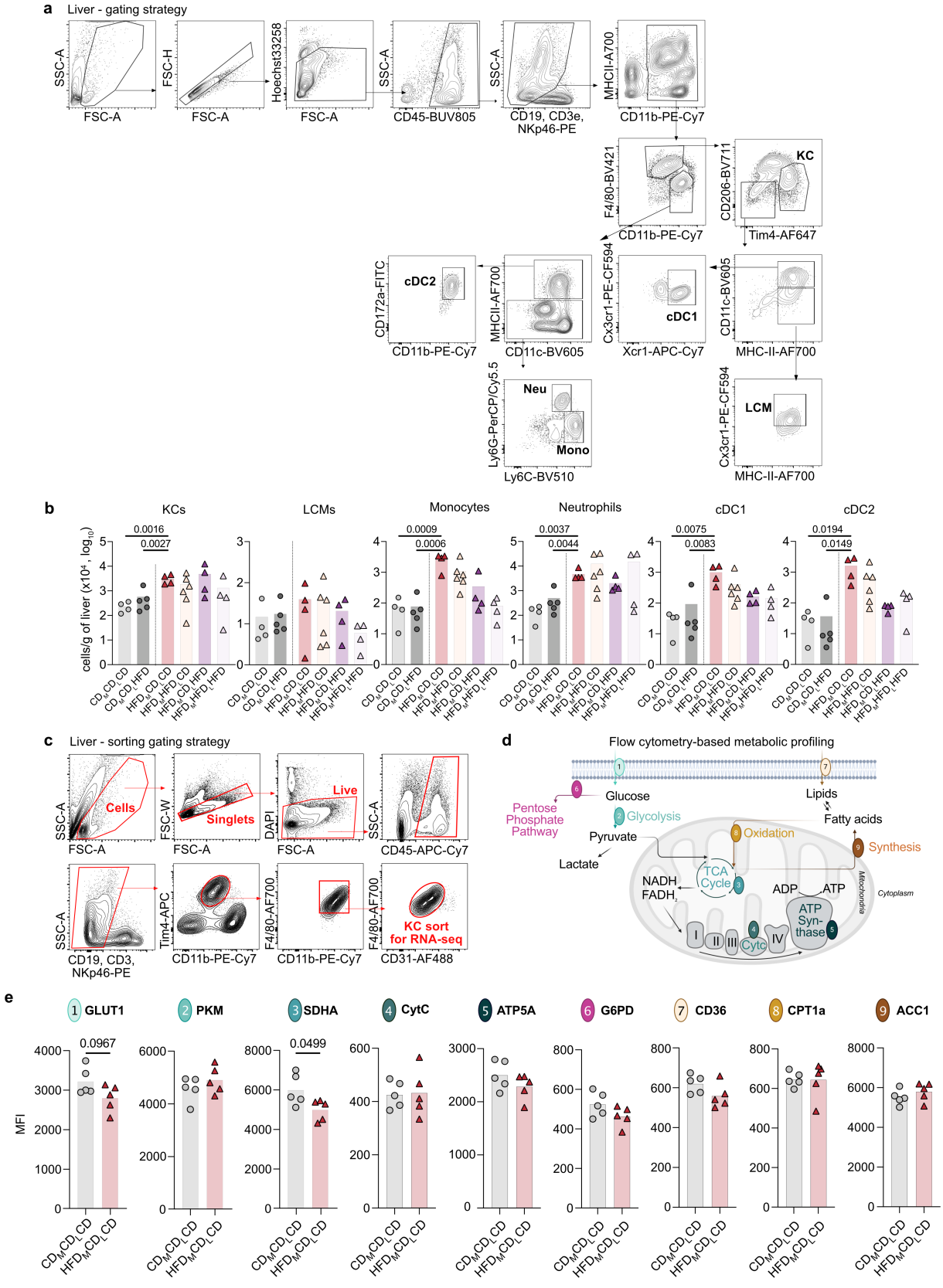

Extended Data Fig. 2 | See next page for caption.

Extended Data Fig. 2 | Flow cytometry analysis, FACS gating strategy and metabolic profiling of KCs and liver myeloid cells. a, Flow cytometry gating strategy for KCs, Liver Capsular Macrophages (LCM), classical Dendritic Cells 1 and 2 (cDC1, cDC2), monocytes (Mono) and neutrophils (Neu). **b**, Cell number of different myeloid populations per gram of liver tissue quantified by flow cytometry. n = 4, 5, 4, 6, 4, 4 mice for CD_MCD_LCD, CD_MCD_LHFD, HFD_MCD_LCD, HFD_MHFD_LCD, HFD_MCD_LHFD, HFD_MHFD_LHFD groups, respectively, on 8 experimental days. Bar graphs show the means. One-way ANOVA – Tukey's multiple comparison test, comparing and showing significances of only CD_MCD_LCD, CD_MCD_LHFD and HFD_MCD_LCD groups. **c**, Fluorescence activated cell sorting (FACS) gating strategy for sorting KCs for RNA-seq. **d**, Schematic illustration of metabolite transporters and enzymes assessed for the metabolic state of KCs. 1. GLUT1, glucose transporter 1; 2. PKM, pyruvate kinase M; 3. SDHA, succinate dehydrogenase A; 4. Cytc, cytochrome c; 5. ATP5A, ATP synthase F1 subunit alpha; 6. G6PD, glucose-6-phosphate dehydrogenase; 7. CD36, fatty acid translocase; 8. CPT1A, carnitine palmitoyl transferase 1A; 9. ACC1, acetyl-CoA Carboxylase 1. The schematic was created in BioRender. Mass, E. (2025) https://BioRender.com/axc6avr. **e**, Mean Fluorescence Intensity (MFI) of GLUT1, PKM, SDHA, CytC, ATP5A, G6PD, CD36, CPT1a and ACC1 in KCs isolated from 11–13 weeks CD_MCD_LCD and HFD_MCD_LCD mice. n = 5 mice/group on 1 experimental day. Bar graphs show the means. Two-tailed unpaired Student's t-test.

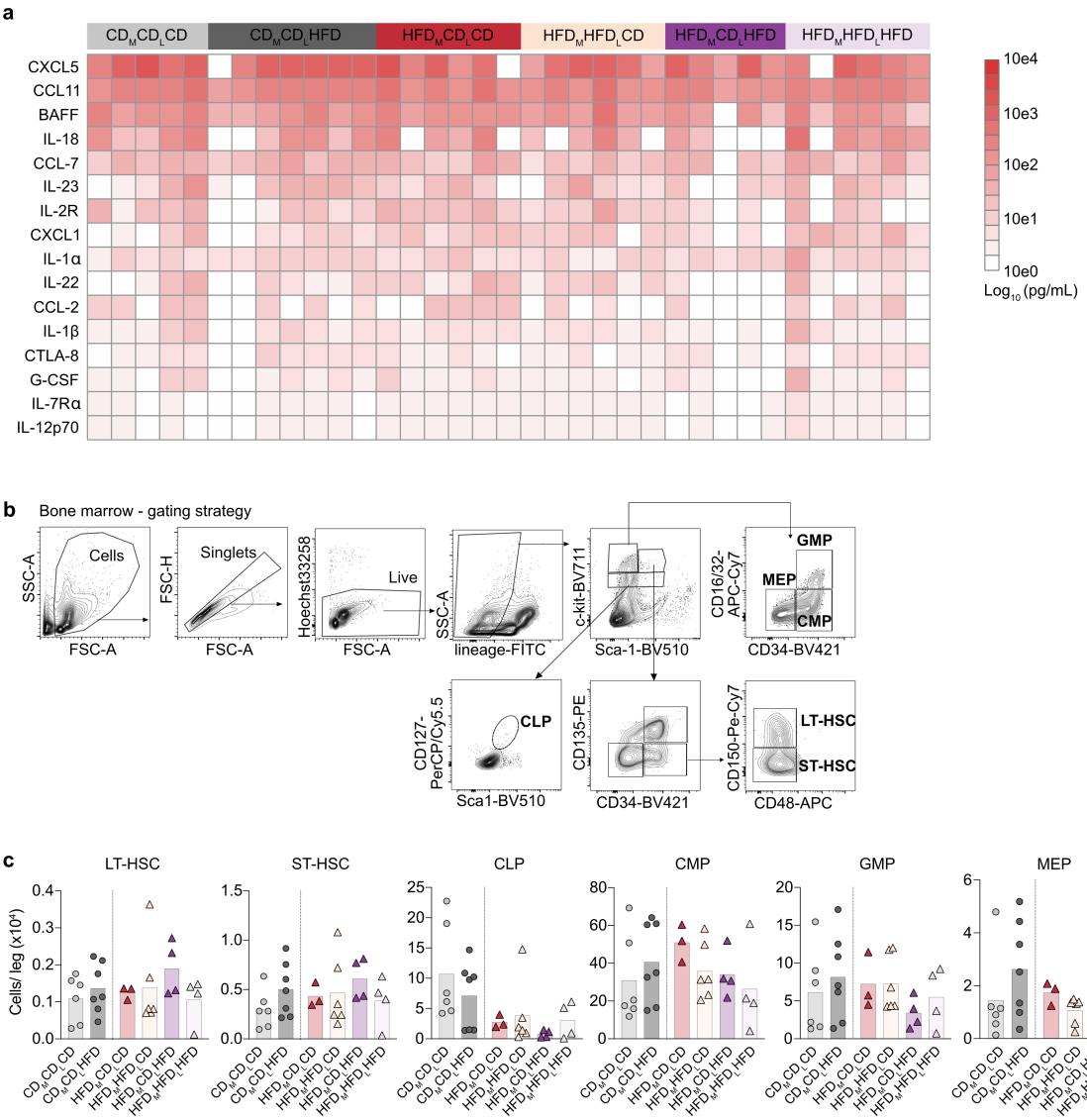

Extended Data Fig. 3 | Characterization of serum and bone marrow immune status in the offspring. a, Heatmap showing log-transformed values of detected cytokines and chemokines in the offspring sera. Each column represents one mouse. n = 5, 7, 6, 6, 5, 6 mice for CD_MCD_LCD, CD_MCD_LHFD, HFD_MCD_LCD, HFD_MHFD_LCD, HFD_MCD_LHFD, HFD_MHFD_LHFD groups, respectively, on 11 experimental days. No significance across conditions using Kruskal-Wallis test. **b**, Flow cytometry gating strategy for analysis of hematopoietic stem and progenitor cells in the bone marrow. LT-HSC, long-term hematopoietic stem cells; ST-HSC, short-term hematopoietic stem cells; GMP, granulocyte-macrophage progenitors; MEP, megakaryocyte-erythroid progenitors; CMP, common myeloid progenitors; CLP, common lymphoid progenitors. **c**, Cell number of different hematopoietic stem and progenitor cells quantified by flow cytometry. n = 6, 7, 3, 6, 4, 4 mice for CD_MCD_LCD, CD_MCD_LHFD, HFD_MCD_LCD, HFD_MHFD_LCD, HFD_MCD_LHFD, HFD_MHFD_LHFD groups, respectively, on 11 experimental days. Bar graphs show the means. No significance across conditions using One-way ANOVA – Tukey's multiple comparison test.

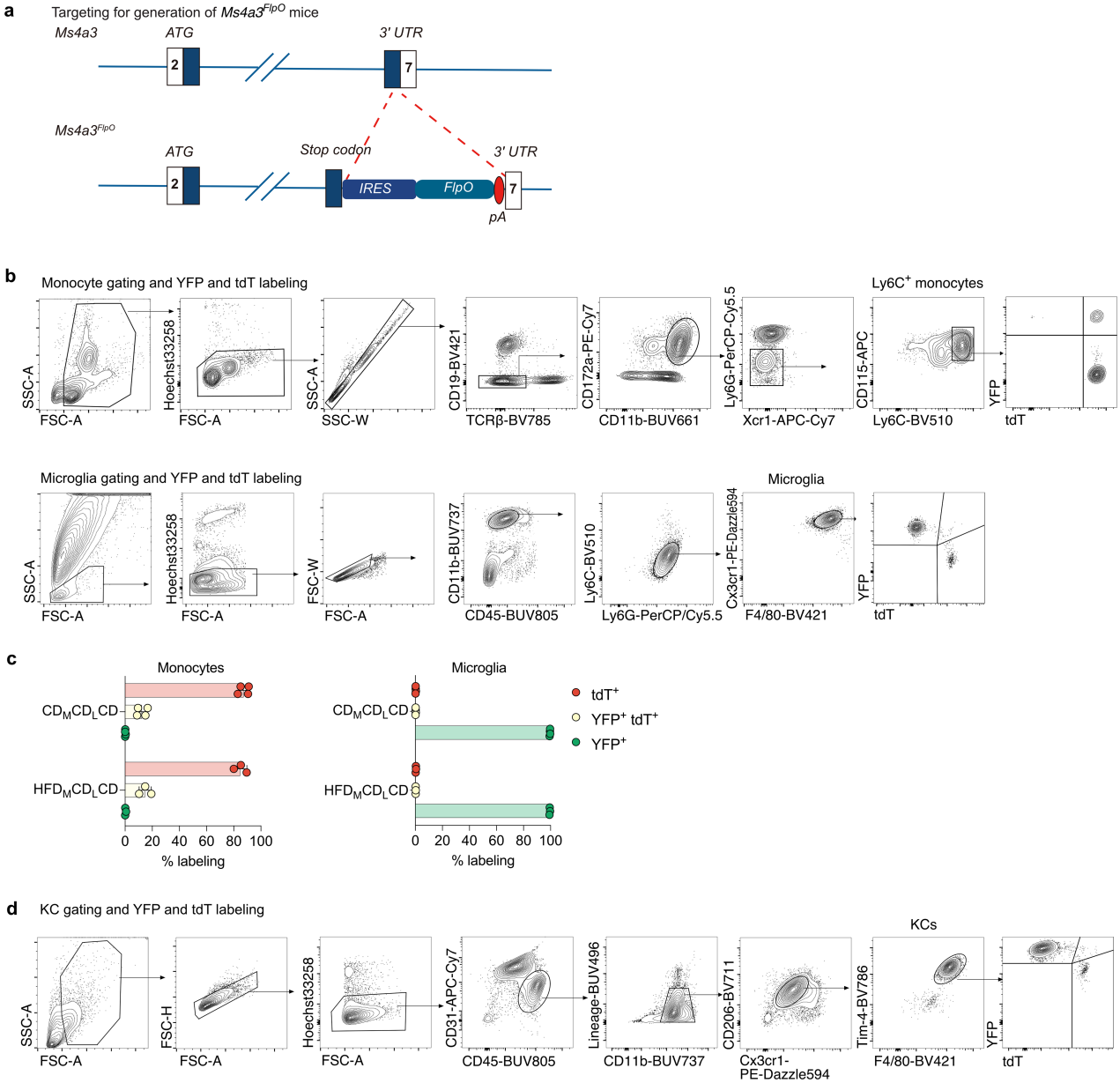

Extended Data Fig. 4 | Analysis of *Tnfrsf11a*^{Cre};*Rosa26*$^{LSL\text{-}YFP}$;*Ms4a3*^{FlpO};*Rosa26*$^{FSF\text{-}tdTomato}$ *double fate mapper* mouse model. a, *Ms4a3* locus indicating targeting strategy. **b**, Flow cytometry gating strategy for blood monocytes and microglia. **c**, Quantification of labelling efficiency of blood monocytes and microglia in 11–12 weeks old maternal lean (CD_MCD_LCD, n = 4 on 2 experimental days) and maternal obese (HFD_MCD_LCD, n = 3 on 2 experimental days) mice. Bar graphs show the mean ± SD. **d**, Flow cytometry gating strategy for KCs.

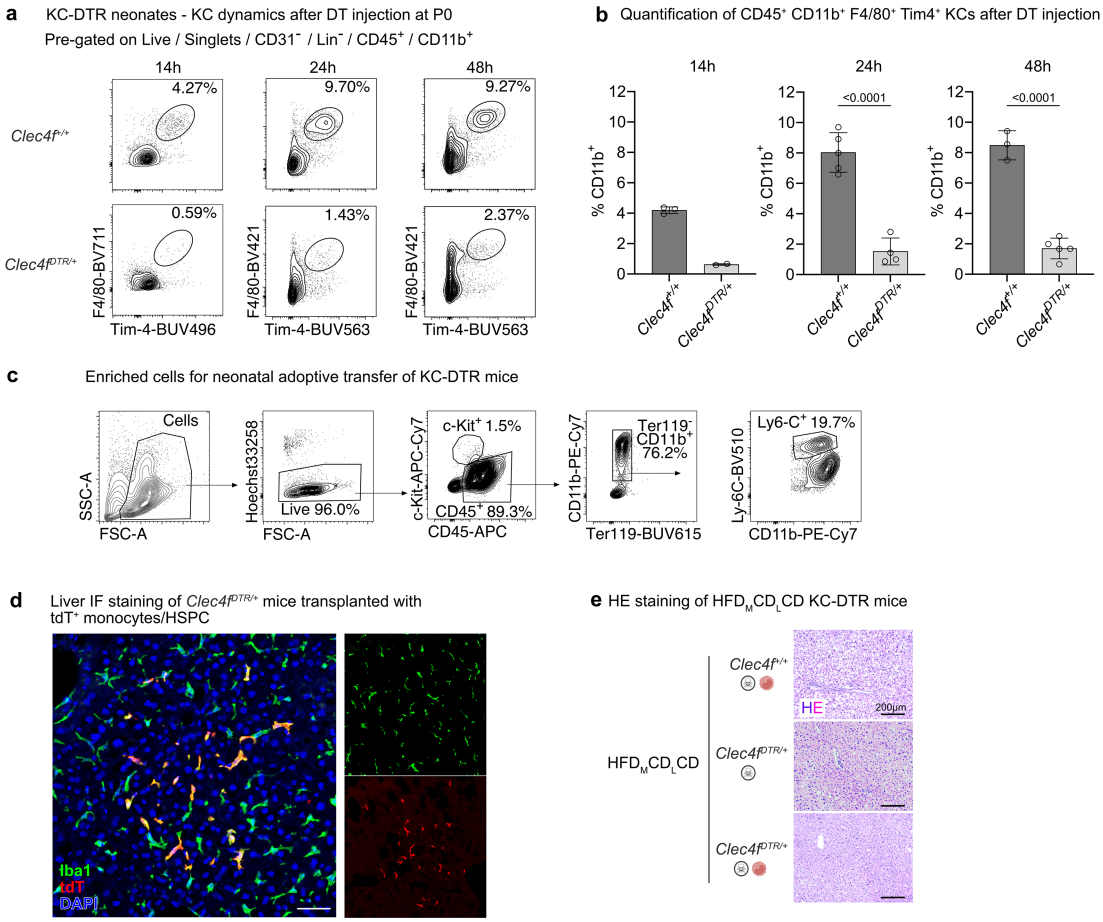

Extended Data Fig. 5 | KC depletion in *Clec4f*$^{DTR/+}$ mouse model. **a**, Representative flow cytometry gating of F4/80$^+$Tim4$^+$ KCs from *Clec4f*$^{+/+}$ and *Clec4f*$^{DTR/+}$ mice 14 h, 24 h and 48 h after diphtheria toxin (DT) injection at P0. **b**, Quantification of F4/80$^+$Tim4$^+$ KCs (gating shown in **a**) in % of CD11b$^+$ cells comparing *Clec4f*$^{+/+}$ and *Clec4f*$^{DTR/+}$ mice 14 h (n = 3 and 2 mice for *Clec4f*$^{+/+}$ and *Clec4f*$^{DTR/+}$, respectively), 24 h (n = 5 and 4 mice for *Clec4f*$^{+/+}$ and *Clec4f*$^{DTR/+}$, respectively) and 48 h (n = 3 and 5 mice for *Clec4f*$^{+/+}$ and *Clec4f*$^{DTR/+}$, respectively) after DT injection at P0. Bar graphs show the mean ± SD. Two-tailed unpaired Student's t-test when sample size is no less than 3. **c**, Flow cytometry analysis of isolated bone marrow monocytes and hematopoietic stem and progenitor cells (HSPCs) from *Rosa26*^{mTmG} mice used for transplanting *Clec4f*$^{+/+}$ and *Clec4f*$^{DTR/+}$ mice 15 h after DT injection. **d**, Immunofluorescence staining of HFD$_M$CD$_L$CD *Clec4f*$^{DTR/+}$ liver at the age of 13 weeks showing the partial replacement of endogenous KCs by tdT$^+$ bone marrow monocytes and HSPCs from *Rosa26*^{mTmG} mice. KCs are shown as Iba1$^+$ and nuclei as DAPI$^+$. Scale bar: 50 µm. Representative image of n = 9 mice on 4 experimental days. **e**, Representative H&E staining of livers in Fig. 2f–h. Scale bar: 200 µm. The illustrations were created in BioRender. Mass, E. (2025) https://BioRender.com/1don7ps.

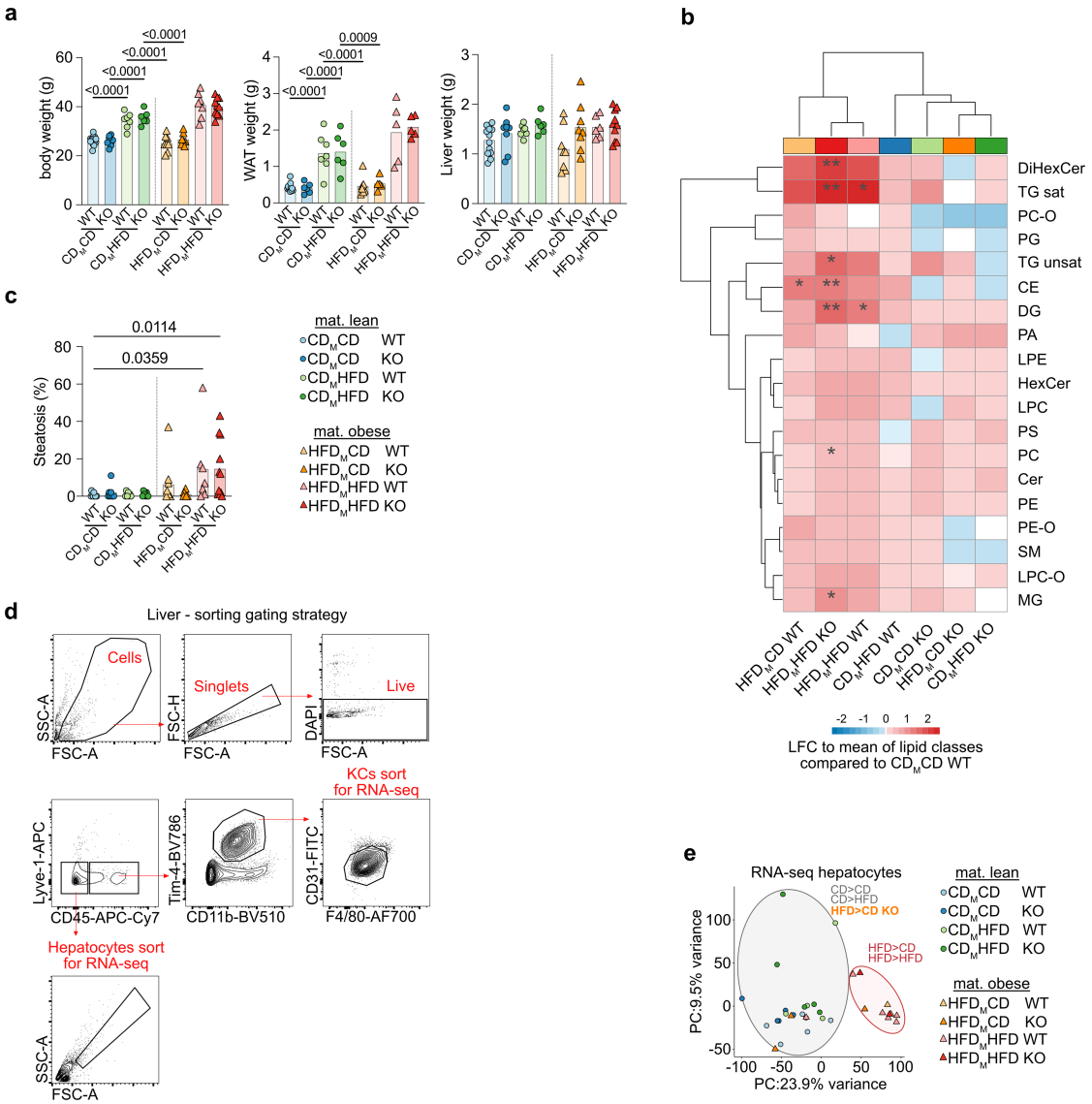

Extended Data Fig. 6 | Characterization of *Hif1α*-WT and *Hif1α*-KO maternal lean and obese offspring. a, Body, WAT and liver weight of 11-week-old offspring. Each circle/triangle represents one mouse. n = 12, 8, 7, 6, 8, 7, 7, 10 mice for CD_MCD WT, CD_MCD KO, CD_MHFD WT, CD_MHFD KO, HFD_MCD WT, HFD_MCD KO, HFD_MHFD WT, HFD_MHFD KO groups, respectively, on 15 experimental days. Bar graphs show the means. One-way ANOVA – Tukey's multiple comparison test. **b**, Heatmap of liver lipidomics in Fig. 3d showing the condition-wise Log-Fold changes (LFC) against the CD_MCD of selected lipid groups. Two-tailed unpaired Student's t-test on the individual coefficients after linear fitting model and multiple testing correction using false discovery rate <0.05 (* = $p < 0.05$, ** = $p < 0.01$, *** = $p < 0.001$). **c**, Pathological scoring of liver steatosis performed on HE stainings. n = 7, 7, 7, 8, 7, 8, 7, 11 mice for CD_MCD WT, CD_MCD KO, CD_MHFD WT, CD_MHFD KO, HFD_MCD WT, HFD_MCD KO, HFD_MHFD WT, HFD_MHFD KO groups, respectively, on 15 experimental days. Bar graphs show the means. One-way ANOVA – Tukey's multiple comparison test. **d**, FACS-gating strategy to sort KCs and hepatocytes for RNA-seq. **e**, RNA-seq of FACS-sorted hepatocytes from all diet groups of *Hif1α*-WT and *Hif1α*-KO mice visualized by PCA. n = 5, 5, 5, 5, 2, 3, 6, 2 mice for CD_MCD WT, CD_MCD KO, CD_MHFD WT, CD_MHFD KO, HFD_MCD WT, HFD_MCD KO, HFD_MHFD WT, HFD_MHFD KO groups, respectively.

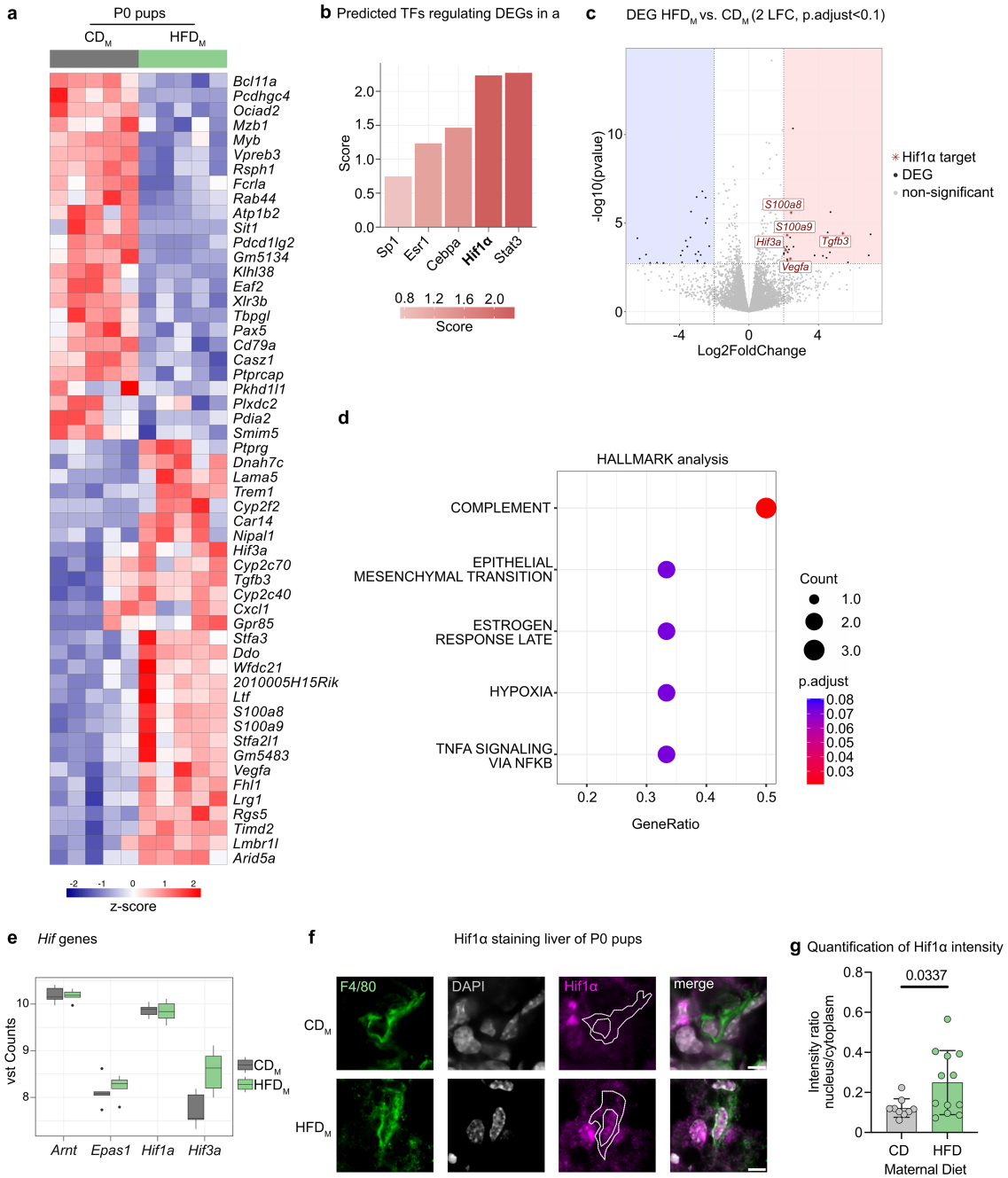

Extended Data Fig. 7 | Transcriptome analysis of KCs isolated from P0 pups. **a**, Heatmap showing scaled expression of DEGs of KCs isolated from pups born to CD-fed (CD_M) or HFD-fed (HFD_M) mothers. n = 5 mice/group. **b**, Transcription factor (TF) activity analysis with genes from **a**. as input. The higher the score is, the higher the predicted activity is of the indicated TF in KCs born to obese mothers. **c**. Volcano plot of DEGs (blue: down, red: up) between P0 KCs born to HFD- and CD-fed mothers. HIF1α targets are highlighted in red. **d**. HALLMARK pathway overrepresentation-analysis of all upregulated DEGs shown in **a**. **e**, Variant supporting counts (vsc) of all *Hif* genes. n = 5 mice/group. Box plots show median with interquartile range and min/max. **f**, Representative images of immunofluorescence staining of HIF1α in F4/80$^+$ KCs in P0 livers born to CD- and HFD-fed mothers. n = 4, 3 P0 pups born to CD-, HFD-fed mothers, respectively, on 3 experimental days. **g**, Quantification of HIF1α intensity in nuclei in % to cytoplasm in F4/80$^+$ KCs comparing P0 pups born to CD- and HFD-fed mothers in **f**. n = 9, 12 cells from P0 pups born to CD-, HFD-fed mothers, respectively. Bar graphs show the mean ± SD. Two-tailed Mann-Whitney test.

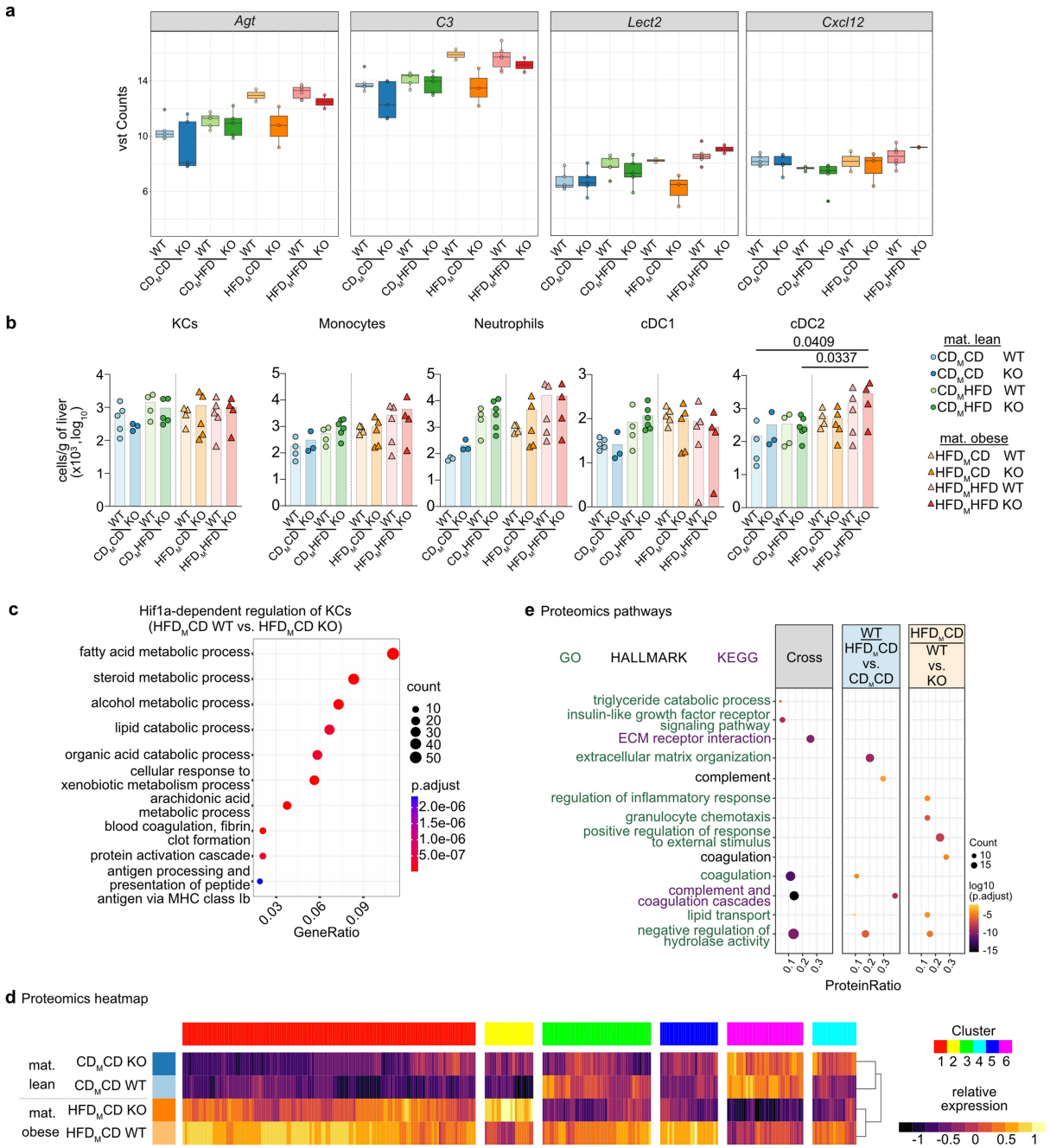

Extended Data Fig. 8 | Characterization of myeloid cell immune infiltration and ex vivo KC proteomics in *Hif1α*-WT and *Hif1α*-KO livers. a, Expression of selected chemo-attractants expressed by hepatocytes across diet groups of HIF1α mouse model. n = 5, 5, 5, 5, 2, 3, 6, 2 mice for CD_MCD WT, CD_MCD KO, CD_MHFD WT, CD_MHFD KO, HFD_MCD WT, HFD_MCD KO, HFD_MHFD WT, HFD_MHFD KO groups, respectively. Box plots show medians with interquartile range and min/max. **b**, Cell number of different myeloid populations per gram of liver tissue quantified by flow cytometry. n = 5, 3, 4, 5, 4, 5, 5, 4 mice for CD_MCD WT, CD_MCD KO, CD_MHFD WT, CD_MHFD KO, HFD_MCD WT, HFD_MCD KO, HFD_MHFD WT, HFD_MHFD KO groups, respectively, on 15 experimental days. Bar graphs show the means. One-way ANOVA – Tukey's multiple comparison test. **c**, Dot plot showing ORA analysis of DEGs comparing HFD_MCD WT versus HFD_MCD KO conditions. **d**, Heatmap showing the relative mean expression and hierarchical clustering of differentially expressed proteins from isolated KCs comparing HFD_MCD WT vs. CD_MCD WT mice, HFD_MCD WT vs. HFD_MCD KO mice, and the overlapping proteins of the two comparisons. Same experiment as Fig. 3h, where selected proteins from the different clusters are displayed. **e**, Dot plot showing enriched pathways of the differentially expressed proteins from Fig. 3g.

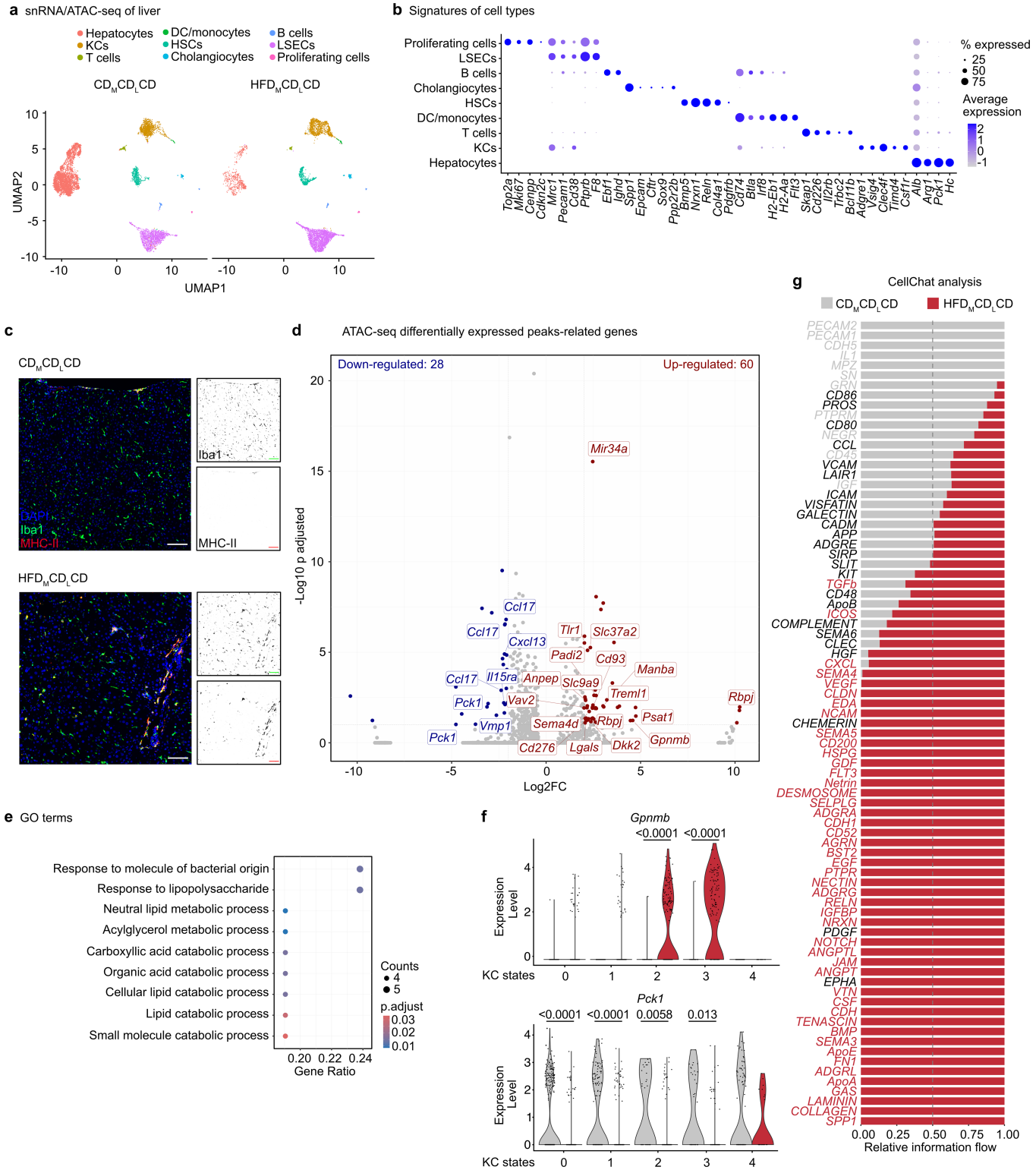

Extended Data Fig. 9 | Single nucleus (sn)RNA/ATAC-seq analysis of CD_MCD_LCD and HFD_MCD_LCD KCs. a, snRNA/ATAC-seq of CD_MCD_LCD and HFD_MCD_LCD livers visualized by Uniform Manifold Approximation (UMAP) showing all liver cell types. **b**, Dot plot showing the genes determining the cell type annotation of identified clusters shown in **a**. **c**, Representative immunofluorescence (IF) staining showing MHC-II expression in the liver of CD_MCD_LCD and HFD_MCD_LCD mice. All KCs and macrophages are labelled with Iba1. scale bar: 200 µm. Representative pictures of n = 11 CD_MCD_LCD and n = 7 HFD_MCD_LCD mice. **d**, Volcano plot showing assigned genes to the differentially detected snATAC-seq peaks between KCs from CD_MCD_LCD and HFD_MCD_LCD livers. **e**, GO term analysis of downregulated genes associated with snATAC-seq peaks. **f**, Violin plots comparing *Gpnmb* (upper) and *Pck1* (lower) expression within all KC states comparing CD_MCD_LCD and HFD_MCD_LCD groups. Two-tailed Wilcoxon Rank Sum test. **g**, CellChat analysis using differentially expressed genes between CD_MCD_LCD and HFD_MCD_LCD KCs as sender molecules and all cell types as receivers. Coloured genes indicate significant ($p < 0.05$) differences of information flow between the conditions tested with Two-tailed Wilcoxon Rank Sum test.

nature portfolio

Corresponding author(s): Elvira Mass

Last updated by author(s): Apr 30, 2025

Reporting Summary

Nature Portfolio wishes to improve the reproducibility of the work that we publish. This form provides structure for consistency and transparency in reporting. For further information on Nature Portfolio policies, see our Editorial Policies and the Editorial Policy Checklist.

Please do not complete any field with "not applicable" or n/a. Refer to the help text for what text to use if an item is not relevant to your study.
For final submission: please carefully check your responses for accuracy; you will not be able to make changes later.

Statistics

For all statistical analyses, confirm that the following items are present in the figure legend, table legend, main text, or Methods section.

n/a	Confirmed	
☐	☒	The exact sample size (*n*) for each experimental group/condition, given as a discrete number and unit of measurement
☐	☒	A statement on whether measurements were taken from distinct samples or whether the same sample was measured repeatedly
☐	☒	The statistical test(s) used AND whether they are one- or two-sided *Only common tests should be described solely by name; describe more complex techniques in the Methods section.*
☒	☐	A description of all covariates tested
☐	☒	A description of any assumptions or corrections, such as tests of normality and adjustment for multiple comparisons
☐	☒	A full description of the statistical parameters including central tendency (e.g. means) or other basic estimates (e.g. regression coefficient) AND variation (e.g. standard deviation) or associated estimates of uncertainty (e.g. confidence intervals)
☐	☒	For null hypothesis testing, the test statistic (e.g. *F*, *t*, *r*) with confidence intervals, effect sizes, degrees of freedom and *P* value noted *Give P values as exact values whenever suitable.*
☒	☐	For Bayesian analysis, information on the choice of priors and Markov chain Monte Carlo settings
☒	☐	For hierarchical and complex designs, identification of the appropriate level for tests and full reporting of outcomes
☒	☐	Estimates of effect sizes (e.g. Cohen's *d*, Pearson's *r*), indicating how they were calculated

Our web collection on statistics for biologists contains articles on many of the points above.

Software and code

Policy information about availability of computer code

Data collection	Flow cytometry data were collected using BD FACSymphony A5 SORP Cytometer with BD FACSDiva version 9.0, ARIA III (BD Bioscience) with BD FACSDiva version 9.0, or Sony ID7000 (Sony) with ID7000 Acquisition and Analysis Software version 2.0.2. Images were acquired on a Axio Lab.A1 microscope (Zeiss) ,Axio Observer Z1 in Apotome mode (Zeiss), or LSM880 (Zeiss) with Zen Blue software. Cytokine multiplex assay data were collected using the Luminex xMAP system with xMAP INTELLIFLEX Software version 1.0. Bulk and single-cell RNA-Sequencing libraries were sequenced using a NextSeq500 (bulk) or NextSeq2000 (single nucleus sequencing) instrument (Illumina). Direct infusion lipidomics was performed using a Thermo Q Exactive Plus spectrometer equipped with the HESI II ion source.
Data analysis	Flow cytometry data were analyzed with FlowJo version v10.9.0. Oil-red-O analysis was quantified using QuPath version 0..5.1. Quantitative analysis of immunofluorescence images was performed using Fiji version 2.7.0. Cytokine multiplex assay results were analyzed with ProcartaPlex Analysis App software version 1.0. RNA-Seq data were analyzed in R environment. Lipidomics raw files were converted to .mzml files and imported into and analyzed by LipidXplorer software v 1.2.8.1 using custom mfql files to identify sample lipids and internal standards. Metabolomics data were analyzed in R environment. Detailed description of analysis methods as well as all packages and versions used for analyses are provided in the Methods section and Table 9.

For manuscripts utilizing custom algorithms or software that are central to the research but not yet described in published literature, software must be made available to editors and reviewers. We strongly encourage code deposition in a community repository (e.g. GitHub). See the Nature Portfolio guidelines for submitting code & software for further information.

Data

Policy information about availability of data

All manuscripts must include a data availability statement. This statement should provide the following information, where applicable:

- Accession codes, unique identifiers, or web links for publicly available datasets
- A description of any restrictions on data availability
- For clinical datasets or third party data, please ensure that the statement adheres to our policy

Transcriptome data have been deposited in NCBI's Gene Expression Omnibus and are accessible through GEO Series accession number GSE237408 (https://www.ncbi.nlm.nih.gov/geo/query/acc.cgi?acc=GSE237408).
Lipidomics data is available at Metabolomics Workbench, Study IDs ST002871 and ST002872 within the project PR001715 (DOI: http://dx.doi.org/10.21228/M81D9R).
Metabolome data are available at Metabolomics Workbench, Study ID ST002754 (DOI: http://dx.doi.org/10.21228/M81D9R).
All pictures used for quantificaiton are available at Bonndata (https://doi.org/10.60507/FK2/PP2MPB).

Research involving human participants, their data, or biological material

Policy information about studies with human participants or human data. See also policy information about sex, gender (identity/presentation), and sexual orientation and race, ethnicity and racism.

Reporting on sex and gender	this study does not include data from human samples
Reporting on race, ethnicity, or other socially relevant groupings	this study does not include data from human samples
Population characteristics	this study does not include data from human samples
Recruitment	this study does not include data from human samples
Ethics oversight	this study does not include data from human samples

Note that full information on the approval of the study protocol must also be provided in the manuscript.

Field-specific reporting

Please select the one below that is the best fit for your research. If you are not sure, read the appropriate sections before making your selection.

☒ Life sciences ☐ Behavioural & social sciences ☐ Ecological, evolutionary & environmental sciences

For a reference copy of the document with all sections, see nature.com/documents/nr-reporting-summary-flat.pdf

Life sciences study design

All studies must disclose on these points even when the disclosure is negative.

Sample size	G*Power was used to estimate the minimum sample size needed. Final sample size was based on the availability of resources and the goal of achieving reproducibility across independent experiments. The chosen sample sizes allowed for appropriate statistical analyses and demonstrated consistent reproducibility of results across replicates.
Data exclusions	Outliers were identified using the ROUT function in Prism 10. Outliers of RNA-seq samples were excluded due to low quality, here the specific outliers and how the data was analyzed are described in the Methods section.
Replication	Cohorts of mice have been generated over several years, always comparing littermates, and have been replicable. Detailed cohort collection is indicated in the figure legends.
Randomization	The maternal mice used in our study were randomly selected from the available cohort without any pre-selection criteria and put randomly into either control diet (CD) or high-fat diet (HFD). To further standardize and minimize potential confounding factors, litters from different mothers were cross-fostered to the same foster mother, whenever possible. Additionally, to ensure that offspring within the same dietary groups (CD or HFD) maintained a similar microbiome, we collected bedding material with feces from all cages, mixed it thoroughly, and redistributed it to all cages within the respective diet group. This approach aimed to harmonize the microbiome across animals within each dietary group. These measures, combined with focusing exclusively on male mice, ensured a robust and unbiased experimental design while addressing our study's objectives.
Blinding	Due to the objective manner of analysis, researchers were not blinded in these studies.

Reporting for specific materials, systems and methods

We require information from authors about some types of materials, experimental systems and methods used in many studies. Here, indicate whether each material, system or method listed is relevant to your study. If you are not sure if a list item applies to your research, read the appropriate section before selecting a response.

Materials & experimental systems

n/a	Involved in the study
☐	☒ Antibodies
☒	☐ Eukaryotic cell lines
☒	☐ Palaeontology and archaeology
☐	☒ Animals and other organisms
☒	☐ Clinical data
☒	☐ Dual use research of concern
☒	☐ Plants

Methods

n/a	Involved in the study
☒	☐ ChIP-seq
☐	☒ Flow cytometry
☒	☐ MRI-based neuroimaging

Antibodies

Antibodies used

Antibodies for myeloid cell flow cytometry for WT and Hif1α-KO mice
Antigen Conjugate Clone Source Cat# Final dilution (µg/mL)
CD45 BUV805 30-F11 BD Bioscience 748370 0.25
CD11b PE-Cy7 M1/70 BioLegend 101216 0.25
Tim-4 AF647 RMT4-54 BioLegend 130008 1.25
F4/80 BV421 BM8 BioLegend 123132 0.5
NKp46 PE 29A1.4 BioLegend 137604 1
CD3 PE 145-2C11 BioLegend 100308 1
CD19 PE 1D3/CD19 BioLegend 152408 0.5
Ly6C BV510 HK1.4 BioLegend 128033 0.5
Ly6G PerCP/Cy5.5 1A8 BioLegend 127616 1
Cx3cr1 PE-Dazzle594 SA011F11 BioLegend 149014 0.5
CD11c BV605 N418 BioLegend 117333 1
CD206 BV711 C068C2 BioLegend 141727 1
MHC-II AF700 M5/114.15.2 BioLegend 107622 1.125
CD172a FITC P84 BioLegend 144006 2.5
Xcr1 APC-Cy7 ZET BioLegend 148224 1

Antibodies for HSC flow cytometry for WT and Hif1a KO mice
Antigen Conjugate Clone Source Cat# Final dilution (µg/mL)
CD11b Biotin M1/70 BioLegend 101204 0.625
NKp46 Biotin 29A1.4 BioLegend 137616 2.5
CD3 Biotin 145-2C11 BioLegend 100304 2.5
CD19 Biotin 6D5 BioLegend 115504 1.125
Gr1 Biotin RB6-8C5 BioLegend 108404 1.125
Ter119 Biotin TER-119 BioLegend 116204 2.5
c-Kit (CD117) BV711 2B8 BioLegend 105835 1
Sca-1 BV510 D7 BioLegend 108129 0.5
CD48 AF647 HM48-1 BioLegend 103416 2.5
CD150 PE-Cy7 TC15-12F12.2 BioLegend 115914 0.5
CD16/32 APC-Cy7 93 BioLegend 101328 2
CD34 BV421 MEC14.7 BioLegend 119321 2
CD135 PE A2F10 BioLegend 135306 2
CD127 PerCP/Cy5.5 A7R34 BioLegend 135022 2
Streptavidin FITC BioLegend 405201 5

Antibody for KC sorting for WT and Hif1a KO mice
Antigen Conjugate Clone Source Cat# Final dilution (µg/mL)
CD45 APC-Cy7 30-F11 BioLegend 103116 0.5
CD11b PE-Cy7 M1/70 BD Bioscience 552850 0.25
Tim4 BV786 21H12 BD Bioscience 742778 1
F4/80 AF700 BM8 BioLegend 123130 1.67
NKp46 PE 29A1.4 BioLegend 137604 1
CD3 PE 145-2C11 BioLegend 100308 1
CD19 PE 1D3/CD19 BioLegend 152408 0.5
CD31 AF488 MEC13.3 BioLegend 102514 5

Antibody for blood monocyte flow cytometry for double-fate mapper mice
Antigen Conjugate Clone Source Cat# Final dilution (µg/mL)
CD19 BV421 6D5 BioLegend 115537 1

TCRβ Biotin H57-597 BioLegend 109204 1.125
CD172a PE-Cy7 P84 BioLegend 144008 0.5
CD11b BUV661 M1/70 BD Bioscience 612977 1
Ly6G PerCP-Cy5.5 1A8 BioLegend 127616 1
Xcr1 APC-Cy7 ZET BioLegend 148224 1
Ly6C BV510 HK1.4 BioLegend 128033 1
CD115 APC AFS98 BioLegend 135510 1
Streptavidin BV785 BioLegend 405249 1

Antibody for KC flow cytometry for double-fate mapper mice
Antigen Conjugate Clone Source Cat# Final dilution (µg/mL)
CD31 APC-Cy7 MEC13.3 BioLegend 102534 1
CD45 BUV805 30-F11 BD Bioscience 748370 0.25
CD11b BUV737 OX-42 BD Bioscience 612800 1
Ter119 Biotin TER-119 BioLegend 116204 2.5
TCRβ Biotin H57-597 BioLegend 109204 1.125
CD19 Biotin 6D5 BioLegend 115504 1.125
Siglec-F Biotin S17007L BioLegend 155512 2.5
Nkp46 Biotin 29A1.4 BioLegend 137616 2.5
Cx3cr1 PE-Dazzle594 SA011F11 BioLegend 149014 0.5
CD206 BV711 C068C2 BioLegend 141727 1
F4/80 BV421 BM8 BioLegend 123132 0.5
Tim-4 BV786 21H12 BD Bioscience 742778 1
Streptavidin BUV496 BD Bioscience 612961 0.25

Antibody for microglia flow cytometry for double-fate mapper mice
Antigen Conjugate Clone Source Cat# Final dilution (µg/mL)
CD45 BUV805 30-F11 BD Bioscience 748370 0.25
CD11b BUV737 OX-42 BD Bioscience 612800 1
Ly6C BV510 HK1.4 BioLegend 128033 1
Ly6G PerCP/Cy5.5 1A8 BioLegend 127616 1
Cx3cr1 PE-Dazzle594 SA011F11 BioLegend 149014 0.5
F4/80 BV421 BM8 BioLegend 123131 0.5

Antibody for KC metabolic profiling panel
Antigen Conjugate Clone Source Cat# Final dilution (µg/mL)
CD45 BUV805 30-F11 BD Biosciences 568336 0.5
CD11b BUV737 M1/70 BD Biosciences 612800 0.5
F4/80 BUV395 BM8 eBioscience 363-4801-82 0.5
CD64 BV711 X54-5/7.1 Biolegend 139311 2
Tim4 BUV496 RMT4-54 BD Biosciences 750515 0.5
Vsig4 PE-efluor 610 NLA14 eBioscience 61-5752-82 0.125
Clec2 APC 17D9 Biolegend 146106 0.125
CD36 AF700 HM36 eBioscience 56-0362-82 2
CD98 BUV615 H202-141 BD Biosciences 752360 2
CD31 BUV661 390 BD Biosciences 741505 1
MHC-II SparkBlue550 M5/114.15.2 Biolegend 128033 0.5
Ly6C BV510 HK1.4 Biolegend 128033 0.5
Glut1 DL405 DyLight® 405 Conjugation Kit (Fast) - Lightning-Link® Abcam ab201798
EPR3915 Abcam ab252403 1.25
PKM PE PE / R-Phycoerythrin Conjugation Kit - Lightning-Link® Abcam ab102918
EPR10138(B) Abcam ab206129 0.625
SDHA AF647 Alexa Fluor® 647 Conjugation Kit (Fast) - Lightning-Link® Abcam ab269823
EPR9043(B) Abcam ab240098 0.625
CPT1a PE-Cy5 PE/Cy5® Conjugation Kit - Lightning-Link® Abcam ab102893
EPR21843-71-2F Abcam ab235841 0.625
Acc1 AF488 Alexa Fluor® 488 Conjugation Kit (Fast) - Lightning-Link® Abcam ab236553
EPR23235-147 Abcam ab272704 2.5
CytC Pe-Cy7 PE/Cy7® Conjugation Kit - Lightning-Link® Abcam ab102903
7H8.2C12 Abcam ab237966 1.25
ATP5a PerCP-Cy5.5 PerCP/Cy5.5® Conjugation Kit - Lightning-Link® Abcam ab102911
EPR13030(B) Abcam ab231692 5
G6PD APC-Cy7 APC/Cy7® Conjugation Kit - Lightning-Link® Abcam ab102859
EPR20668 Abcam ab231828 1.25

Antibody for immunofluorescence staining
Antigen Conjugate Clone Source Cat# Final dilution (µg/mL)
Hif1α Purified Polyclonal Novus Biologicals NB100-479SS 10
Tim-4 PE RMT4-54 Biolegend 130005 2
Iba1 Purified Polyclonal Novus Biologicals NB100-1028 0.5
RFP Purified Polyclonal Rockland 600-401-379 1
F4/80 Purified BM8 Biolegend 123101 5
Iba1 Purified EPR16589 Abcam ab178847
MHC-II Purified M5/114.15.2 Biolegend 107601
Donkey anti-rabbit AF488 Invitrogen A-21206 2
Donkey anti-rabbit AF555 Invitrogen A-31572 2

Donkey anti-goat AF647 Invitrogen A-21447 2
Donkey anti-rat AF647 Invitrogen A-78947 2
DAPI Biolegend 422801 0.5

Antibody for enrichment and flow cytometry analysis of monocyte and HSPCs
Antigen Conjugate Clone Source Cat# Final dilution (µg/mL)
Ly-6G Biotin 1A8 BioLegend 127603 2.5
CD3 Biotin 145-2C11 BioLegend 100304 2.5
CD19 Biotin 6D5 BioLegend 115504 1.125
Ter119 Biotin TER-119 BioLegend 116204 2.5
Nkp46 Biotin 29A1.4 BioLegend 137616 2.5
F4/80 Biotin BM8 BioLegend 123105 2.5
c-Kit (CD117) APC-Cy7 2B8 BioLegend 105826 1
CD45 APC 30-F11 BioLegend 103112 0.5
CD11b PE-Cy7 M1/70 BD Bioscience 552850 0.25
Ter119 BUV615 Ter-119 BD Bioscience 751534 0.5
Ly6C BV510 HK1.4 Biolegend 128033 0.5

Validation

All antibodies for flow cytometry used in this study were purchased from BD Bioscience and BioLegend. All antibodies used were characterized and validated by providers.

Animals and other research organisms

Policy information about studies involving animals; ARRIVE guidelines recommended for reporting animal research, and Sex and Gender in Research

Laboratory animals	As wildtype strain, C57BL/6JRcc was used from the in-house mouse facility. To generate Hif1aflox/flox; LysMCre/+ the Hif1aflox/flox (JAX stock #007561) and LysMCre/+ (JAX stock #004781) were used. To generate the double fate-mapper Tnfrsf11aCre (from Yasuhiro Kobayashi); Rosa26LSL-YFP (JAX stock #006148); Ms4a3FlpO (from Florent Ginhoux); Rosa26FSF-tdTomato (JAX stock #032864), we bred Tnfrsf11aCre/+; Rosa26FSF-tdTomato/FSF-tdTomato animals with Ms4a3FlpO; Rosa26LSL-YFP/LSL-YFP animals. All mice were analyzed between 11-13 weeks of age.
Wild animals	The study did not involve wild animals
Reporting on sex	For all experiments of the offspring, males were analyzed with the exception of the double fate-mapper and ex vivo isolated hepatocytes and macrophages where both males and females were used at the age of 11-12 weeks.
Field-collected samples	No field-collected samples are included
Ethics oversight	All investigations concerning mouse work have local approval and all procedures conform to the guidelines from Directive 2010/63/EU of the European Parliament on protecting animals used for scientific purposes. In detail, all animal experiments were conducted according to the German law of animal protection and in agreement with the approval of the local institutional animal care committee (Landesamt für Natur, Umwelt und Verbraucherschutz (LANUV), North Rhine-Westphalia, Az 81-02.04.2019.A146 and Az 2024.A314). Mice were housed under specific pathogen-free conditions with 12-h light/dark cycle, at 21°C, 55% relative humidity, and with food and water provided ad libitum.

Note that full information on the approval of the study protocol must also be provided in the manuscript.

Flow Cytometry

Plots

Confirm that:

☒ The axis labels state the marker and fluorochrome used (e.g. CD4-FITC).

☒ The axis scales are clearly visible. Include numbers along axes only for bottom left plot of group (a 'group' is an analysis of identical markers).

☒ All plots are contour plots with outliers or pseudocolor plots.

☒ A numerical value for number of cells or percentage (with statistics) is provided.

Methodology

Sample preparation

Adult mice were anesthetized and perfused with ice-cold PBS. Postnatal day (P)0 mice were killed by decapitation. For flow cytometry analysis of hepatic myeloid cells, 200 to 300 mg of adult or half or P0 liver was collected, cut into small pieces, and incubated in a digestion mix (PBS containing 1 mg/ml collagenase D (Roche, Cat# 11088858001), 100 U/ml DNase I (Sigma-Aldrich, Cat# DN25), 2.4 mg/ml of dispase (Gibco Cat# 17105041) and 3% fetal calf serum (FCS) (Invitrogen) for 30 min at 37 °C before mechanical disruption through a 100 µm filter. The cell suspension was diluted in 3 ml of FACS buffer (0.5 % BSA, 2 mmol EDTA in PBS) and centrifuged at 50x g for 3 min to remove hepatocytes. Then, the supernatant was collected and centrifuged at 370 x g for 7 min, 4 °C. For bone marrow, one leg was isolated, and both the tibia and femur were cleaned from surrounding tissues and cut at the ends. The bones were flushed with 5 ml of ice-cold FACS buffer. Cells were centrifuged at 370 x g for 7 min, 4 °C. Pellet was resuspended in red blood cell lysis buffer (155 mM NH4Cl, 12 mM NaHCO3

	and 0.1 mM EDTA) and incubated for 3 min on ice. Then, 5 ml of FACS buffer were added, cells were resuspended and centrifuged at 370 x g for 7 min, at 4 °C. Tissue pellet was resuspended in FACS buffer containing purified anti-CD16/32 and 2% rat serum (liver) or 2% rat serum only (bone marrow) and incubated for 15 min at 4 °C. Samples were immunostained with antibody mixes for 30 min at 4 °C. The complete list of antibodies used can be found in the "Material and Methods" session of the manuscript. Data were acquired with FACSymphonyTM A5 (BD Biosciences) or LSRII and analyzed in FlowJoTM Software. For sorting of Kupffer cells and hepatocytes, the liver cell suspension was prepared as described above with the following modifications: First, 1 ml of twice-concentrated digestion mix was used for tissue digestion. Second, digestion was performed at room temperature, and centrifugation at 50 x g for 3 min was omitted to retain hepatocytes. Finally, all steps were performed with buffers containing 1 mM of flavopiridol (Sigma-Aldrich, F3055).
Instrument	Flow cytometry samples were analysed at BD FACSymphony A5 SORP Cytometer or Sony ID7000. For sorting experiments, cells were sorted at FACSAria III (BD Bioscience) cell sorter.
Software	Data were collected with BD Diva software (BD Biosciences) or Sony ID7000 system software (Sony) and analyzed with FlowJo
Cell population abundance	The purity of sorted samples was analyzed by flow cytometry on the same instruments used for sorting.
Gating strategy	Gating strategies for all populations can be found in the Extended Data Figures.

☒ Tick this box to confirm that a figure exemplifying the gating strategy is provided in the Supplementary Information.